



Calhoun: The NPS Institutional Archive
DSpace Repository

Theses and Dissertations

1. Thesis and Dissertation Collection, all items

2005-09

Analysis of 2-axis pencil beam sonar
microbathymetric measurements of mine
burial at the Martha's Vineyard Coastal Observatory

Gotowka, Brendan Reed.

Monterey California. Naval Postgraduate School

<http://hdl.handle.net/10945/1736>

This publication is a work of the U.S. Government as defined in Title 17, United States Code, Section 101. Copyright protection is not available for this work in the United States.

Downloaded from NPS Archive: Calhoun



Calhoun is the Naval Postgraduate School's public access digital repository for research materials and institutional publications created by the NPS community. Calhoun is named for Professor of Mathematics Guy K. Calhoun, NPS's first appointed -- and published -- scholarly author.

Dudley Knox Library / Naval Postgraduate School
411 Dyer Road / 1 University Circle
Monterey, California USA 93943

<http://www.nps.edu/library>

ANALYSIS OF 2-AXIS PENCIL BEAM SONAR MICROBATHYMETRIC
MEASUREMENTS OF MINE BURIAL AT THE MARTHA'S VINEYARD
COASTAL OBSERVATORY

by

Brendan Reed Gotowka

B.S., United States Naval Academy (2003)

Submitted in partial fulfillment of the requirements for the degree of

MASTERS OF SCIENCE
at the
MASSACHUSETTS INSTITUTE OF TECHNOLOGY
and the
WOODS HOLE OCEANOGRAPHIC INSTITUTION

September 2005

© Brendan Reed Gotowka, 2005. All rights reserved.

The author hereby grants to MIT, WHOI, and the United States Navy permission
to reproduce and to distribute copies of this thesis document in whole or in part.

Author.....
Joint Program in Applied Ocean Science and Engineering
Massachusetts Institute of Technology and Woods Hole Oceanographic Institution

Certified by.....
Peter A. Traykovski
Associate Scientist, Woods Hole Oceanographic Institution
Thesis Supervisor

Certified by.....
Arthur B. Baggeroer
Ford Professor of Engineering
Secretary of the Navy / Chief of Naval Operations Chair for Ocean Science
Massachusetts Institute of Technology and Woods Hole Oceanographic Institute
Thesis Reader

Approved by.....
Mark A. Grosenbaugh
Chairman, Joint Committee for Applied Ocean Science and Engineering
Massachusetts Institute of Technology and Woods Hole Oceanographic Institution

ANALYSIS OF 2-AXIS PENCIL BEAM SONAR MICROBATHYMETRIC
MEASUREMENTS OF MINE BURIAL AT THE MARTHA'S VINEYARD
COASTAL OBSERVATORY

By

Brendan Reed Gotowka

Submitted in partial fulfillment
of the requirements for the degree of
Master of Science

at the

MASSACHUSETTS INSTITUTE OF TECHNOLOGY

and the

WOODS HOLE OCEANOGRAPHIC INSTITUTION

September 2005

ABSTRACT

The changing state of warfare has driven the US Navy's area of operations closer to shore into littoral coastal waters. Mine Warfare has been proven as an extremely effective means of battlespace control in these waters. Mines can be inexpensively mass produced and rapidly deployed over large areas. The most common type of mine in use is the bottom placed mine, an object with simple geometry that sits on the seafloor. These mines often exhibit scour induced burial below the seafloor, making detection through traditional mine hunting methods difficult or impossible, while the mines themselves remain lethal. The Office of Naval Research (ONR) has developed a computer model that predicts the extent of mine burial to aid mine hunting and mine clearing operations. Investigations under ONR's Mine Burial Program are presently being conducted to calibrate and validate this model.

This thesis uses data from the deployment of an acoustically instrumented model mine near the Martha's Vineyard Coastal Observatory in part of a larger, 16 total object investigation. A 2-axis pencil beam sonar was deployed concurrently with the mine to obtain microbathymetric measurements of the scour pit development and the progression of mine burial. Data correction techniques to correct for beam pattern induced bathymetry errors and a transformed coordinate system are detailed within. An analysis of scour pit dimensions includes scour depth, area, and volume as well as a look into percent burial by depth as a characteristic measurement important for operational mine hunting. The progression of mine burial is related to the wave climate, unsteady flow hydrodynamic forcing, and bed-load transport. The analysis examines the relative roles of these mechanisms in the scour-infill-bury process.

Thesis Supervisor: Dr. Peter A. Traykovski

Title: Associate Scientist

ACKNOWLEDGEMENTS

My most gracious thanks are extended to my thesis advisor, Peter Traykovski, for his professional involvement during my short time in the Joint Program. His wise guidance, infinite patience, and kind support were invaluable, and I have learned a great deal about the actual scientific process of Oceanography from him. I would be remiss without also extending thanks to Arthur Baggeroer, my academic advisor and the acknowledged “father” of Naval Officer involvement in the Joint Program.

My opportunity to participate in graduate studies at MIT and WHOI was made possible through the Secretary of the Navy’s Program in Oceanography and Oceanographic Engineering. I wish to thank the US Navy for this opportunity.

Finally, I would like to thank my family, especially my sister Erin, for their support, which was essential to my successful completion of this endeavor, and made it possible for me to fully enjoy my short time in Boston and Woods Hole.

TABLE OF CONTENTS

	Page
1. INTRODUCTION	
1.1 Background.....	8
1.2 Review of Previous Mine Burial Studies.....	12
1.2.1 Laboratory Experiments.....	12
1.2.2 <i>In Situ</i> Field Deployments.....	14
1.2.3 IRB/MVCO Deployments.....	15
1.3 Chapter Preview.....	18
2. DEPLOYMENT DESCRIPTION	
2.1 Martha's Vineyard Coastal Observatory.....	19
2.2 Instruments Used.....	21
2.2.1 Acoustic Instrumented Mine.....	21
2.2.2 Rotary 2-Axis Pencil Beam Sonar.....	25
2.2.3 Additional Mine Deployment.....	27
2.3 Environmental Conditions.....	30
2.3.1 Oceanographic Conditions.....	30
2.3.2 Seabed Characteristics – Large and Small Scale Bedforms.....	33
3. DATA SET POST PROCESSING CORRECTIONS	
3.1 Beam Pointing Corrections.....	35
3.1.1 Motivation for Corrections.....	35
3.1.2 Geometric Correction Technique.....	40
3.2 Pole Lean Corrections.....	46
3.2.1 Motivation for Corrections.....	46
3.2.2 Correction Technique Theory.....	48
3.2.3 Numerical Transformation Correction Technique.....	50
4. SCOUR PIT DIMENSION RESULTS	
4.1 Scour Pit Depth.....	56
4.2 Scour Pit Area and Volume.....	60
4.2.1 Scour Pit Surface Area and Volume.....	60
4.2.2 Scour Pit Area versus Depth.....	62
4.3 Burial by Depth.....	67
4.3.1 Burial by Maximum Scour Pit Depth.....	67
4.3.2 Burial by Mean Scour Pit Depth.....	69
4.3.3 Burial by Mine Height.....	71
5. DISCUSSION and CONCLUSION	
5.1 Hydrodynamic Mine Forcing and Bed-Load Flux.....	74
5.1.1 Inertial and Drag Hydrodynamic Forces on the Mine....	74
5.1.2 Wave Averaged Net Bed-Load Flux.....	78
5.2 Scour Pit Progression during Storm Events.....	85
5.3 Conclusions.....	94
6. BIBLIOGRAPHY.....	96

LIST OF FIGURES

	Page
2.1 Martha's Vineyard Coastal Observatory.....	20
2.2 Optically Instrumented Mine.....	22
2.3 Acoustically Instrumented Mine.....	23
2.4 MVCO 12-m Node.....	28
2.5 MVCO Significant Wave Height History.....	31
2.6 MVCO Significant Wave Height during Deployment.....	32
2.7 MVCO RMS Bottom Velocity.....	33
3.1 Beam Pointing Error Schematic.....	36
3.2 Theoretical and Actual Beam Pointing Errors.....	38
3.3 Measured and Returned 2-Axis Pencil Beam Beampattern.....	40
3.4 Beam Pointing Trigonometry Schematic.....	41
3.5 Local Surface Normals.....	42
3.6 Trigonometry to Find α Schematic.....	42
3.7 Theoretical and Actual Beam Pointing Corrections.....	45
3.8 Shifted Coordinate System Schematic.....	47
3.9 Original Returned Sonar Measurements.....	48
3.10 Standard Deviation of Rotational Angles.....	51
3.11 X- and Y- Axes Rotation Angles.....	52
3.12 Corrected Sonar Measurements.....	53
3.13 Difference between Original and Corrected Sonar Measurements..	54
4.1 Mean and Maximum Scour Pit Depth and Wave Height.....	56
4.2 Scour Pit Surface Area, Volume, and Wave Height.....	60
4.3 Scour Pit Area at Differing Depths.....	63
4.4 Scour Pit Area at 35 cm Depth and Wave Height.....	64
4.5 Percent Burial by Depth from Maximum Scour Depth and Mean and Maximum Scour Pit Depth.....	68
4.6 Percent Burial by Depth from Mean Scour Depth and Mean and Maximum Scour Pit Depth.....	70
4.7 Percent Burial by Depth from Mine Height.....	72
5.1 Drag and Inertial Forces and Water Velocities.....	77
5.2 Bed-Load and Suspended Sediment Transport Flux.....	82
5.3 Bed-Load and Suspended Sediment Transport Flux versus Total Bottom Velocity.....	84
5.4 Scour Pit Progression during the First Storm.....	86
5.5 Scour Pit Progression during the Second Storm.....	88
5.6 Scour Pit Progression during the Third Storm.....	91

LIST OF TABLES

	Page
4.1 Scour Pit Mean and Maximum Depths.....	58
4.2 Scour Pit Surface Area, 35 cm Depth Area, and Volume Dimensions.....	65
5.1 Scour Pit Dimensions during the First Storm.....	87
5.2 Scour Pit Dimensions during the Second Storm.....	90
5.3 Scour Pit Dimensions during the Third Storm.....	93

1. INTRODUCTION

1.1 Background

The nature of warfare has changed since the end of the Cold War. The Navy no longer encounters enemies in large scale strategic battlefields on the open ocean. The blue-water navies of the past are not effective in the current changing geopolitical situations. The threat against the United States has changed from opposing superpowers to more localized enemies, changing the threats the Navy must protect its forces from, with many more small confrontations in littoral coastal areas.

Mine warfare was proven to be an effective means of battlefield control as early as 1972. U.S. forces mined North Vietnamese ports and shutdown seaborne imports, eliminating an estimated 85% of all imported supplies into North Vietnam (MINWARA News 2004). Since then, technological advances have evolved mine warfare into a dynamic tool which can not only indirectly affect an enemy's capabilities by limiting logistical lines of communications, but also by directly denying access to otherwise available battlespaces. More recently, Iraq deployed a succession of mine barriers from the surf zone to about 25 nautical miles offshore, following the Soviet Mine doctrine, in anticipation of coalition actions in 1991 during operations Desert Shield and Desert Storm. The USS Princeton was disabled by an Iraqi MANTA bottom mine, and the USS

Tripoli was damaged by an Iraqi LUGM-45 moored mine, further highlighting the effectiveness of mine warfare (Gordon and Trainor 1995).

There are a myriad of mine types and shapes with a wide range of deployment and anchoring methods, which all have different target acquisition and detonation schemes. A 1995 world arsenal inventory detailed 158 mine types in 19 different countries. There are three basic categories of sea mines: bottom, moored, and drifting. Drifting mines, though outlawed in 1907, are sometimes still deployed seen by explosive ordinance demolition (EOD) teams. These mines float freely on or near the surface of the water, and are usually contact detonated. Moored mines are buoyant objects tethered to the bottom, which can sometimes break free of their mooring and float on the surface. These can support a wide range of target acquisition systems, from direct contact to magnetic anomalies to activation based on the detection of specific noise frequencies generated by naval vessels. By far, the most common type of mine is the cylindrical bottom mine, which is negatively buoyant and sits on the seabed. These are relatively inexpensive to produce, and can be easily deployed to cover a large area through the use of aircraft and surface vessels (Inman and Jenkins 2002).

Bottom mines often bury partially or completely into the surrounding seafloor, making detection and clearance difficult for naval forces, however not decreasing their lethality. Mines can bury in several different ways. Self burying mines are equipped with control systems to excavate holes for mines to self-bury

into. Impact burial occurs when the bottom consists of low shear strength muds. Bedform migration, the movement of large bathymetric features such as sand bars, will bury large immobile objects. Liquefaction of larger diameter sediments during storms can reduce the shear strength, allowing the mine to sink and bury. Scour induced burial, which will be dealt with here, occurs when water velocities create turbulent vortices around a mine, forming a trough into which the mine falls and is buried by infilling sediment deposition (Mulhearn 1996).

The presence of mines negatively affects naval operations in shallow waters. Before naval battlegroups can enter an area of suspected enemy mining, mine counter measures must first be undertaken. If intelligence sources report the use of bottom mines placed directly on the seafloor, scour and burial of these mines make them harder to detect. In these scenarios Shallow Water Mine Counter Measure operations are forced to change from mine hunting to mine sweeping, or in a worst-case scenario, total area avoidance, tactically denying the use of that area to all naval assets.

The Naval Research Laboratory has created a mine burial prediction model, where time dependent scour-forced burial of bottom placed mines is predicted from numerical oceanographic models and *in situ* measurements of the wave climate, tidal and storm induced bottom currents, sediment properties, and small scale morphological features, when available. Model tests during the early stages of Operation Iraqi Freedom have demonstrated the positive impact mine burial prediction can have on operational needs (Trembanis et al. 2006). It is

now necessary to verify the accuracy of the model through experimental and *in situ* observations of bottom placed mines in a wide range of environmental conditions.

1.2 Review of Previous Mine Burial Studies

The Office of Naval Research has funded both laboratory and field research to gain a better understanding of scour and burial of bottom placed mines and refine the burial prediction model. Several laboratory experiments have described the basic scour and burial characteristics to give a first order guidance to the project. Additionally, a variety of field experiments have generated the information necessary to not only calibrate the model, but also as a comparison to verify the accuracy of the model.

1.2.1 Laboratory Experiments

Laboratory testing has shown that scour and burial of heavy cylindrical objects under progressive waves on a sandy bed is a function of the Keulegan-Carpenter number ($KC = \frac{2\pi\varepsilon}{D}$, where ε is amplitude of the horizontal water

particle excursion, and D is the diameter of the cylinder) and the Shields

parameter ($Sh = \frac{U^2 f}{2gd(\frac{\rho_s}{\rho} - 1)}$, where U is the far field maximum horizontal water

velocity, f is the friction coefficient, g is gravitational acceleration, ρ_s is the cylinder's density, ρ is the water density, and d is mean grain size of the sand).

Four different scour regimes, depending on Keulegan-Carpenter number and Shields parameter values were described. These are no scour, initial scour,

expanded scour, and periodic burial. No scour occurs when the local flow velocity is less than the critical velocity necessary to initiate sediment motion (Voropayev et al. 2003).

The initial scour regime creates a central scour pit symmetric with the longitudinal axis of the cylinder, as well as two smaller pits at the ends of the cylinder, mainly on the onshore side. The scour dimensions do not change greatly over time with constant wave conditions. The expanded scour regime happens when flow conditions have met requirements to form natural ripples in the seabed. The same characteristics as the initial scour regime are seen, however ripples are formed near the wave breaking point onshore of the cylinder, propagating offshore into deep water. The scour pits at the ends of the cylinder merge with the central pit when the ripples reach the cylinder, given that the ripple height is less than the cylinder height exposed above the seafloor. Periodic burial occurs when wave conditions create ripples with heights greater than the exposed diameter. The scour pit progresses through the initial and expanded scour regime. With time, the ripple height increases in size, until it is large enough to bury the cylinder (Voropayev et al. 2003). Field results are expected to be quite different from controlled laboratory experiments, as there is a much larger range of bedform to mine diameter ratios over a variety of sand sizes to consider.

1.2.2 *In Situ* Field Deployments

Field research has been conducted at several locations around the United States for creating time series of post-impact mine scour and burial characteristics to expand upon previous laboratory experiments. A short deployment in shallow water (7 m) off of Panama City, Florida in 1999 showed the advantages of an instrumented mine in measuring scour-induced burial, as well as the limitations of the model mine in use at the time. A longer deployment followed, in 8 m of water off the Scripps Pier in San Diego, California in the summer of 1999. This time, the mine was seen to bury as an apparent result of large scale bedform (i.e. sand bar) migration. During a three-day period at the beginning of the deployment, the mine exhibited some minor scour and burial. Shortly thereafter the mine showed evidence of more significant burial, reaching a maximum of 50% burial on the 35th day of deployment, with the majority of the burial occurring on the seaward side, indicating possible bedform migration. Afterward, the mine episodic uncovering and re-burial until it was retrieved (Richardson et al. 2001).

This led to a deployment in 4 m water depth at East Pass in Destin, Florida, an area with many active sand dunes and a high rate of bedform migration in late 1999. The mine quickly rotated into the prevailing current, and within 11 days the mine became completely buried, remaining so for the duration of the deployment. In the summer of 2000 experiments were conducted in 4.5 m water depth at Duck, North Carolina with the intent of testing equipment and

deployment strategies for future experiments. The site was chosen for the relatively low-energy oceanographic conditions that typically occur during summer months, coinciding with the deployment period. Accelerometer data showed that the mine rolled into a scour pit created around it by mine-wave-current interactions. Bathymetric surveys excluded the contributions from bedform migration to mine movement and burial (Richardson et al. 2003). The conclusions arrived from the Duck deployments led to the development of a new type of instrumented mine, as well as the inclusion of active sonar systems to quantify mine scour and burial.

1.2.3 IRB/MVCO Deployments

One deployment near Indian Rocks Beach (IRB) in Tampa Bay, Florida in early 2003 and four sets of deployments at the Martha's Vineyard Coastal Observatory (MVCO) near Edgartown, Massachusetts from 2001-2004 were the result of findings from previous deployments detailed above. The IRB deployment was in approximately 12 m water depth 10 km offshore with four acoustically instrumented mines and six optically instrumented mines which provide time dependent scour characteristics. Wave and current data was collected from bottom mounted instruments and wave buoys, and extensive sediment surveys have also been conducted. These measurements will be used to predict burial by wave induced scour, and compared with mine measurements

(Trembanis et al. 2006; Richardson et al. 2004). Final analysis of these deployments is still being conducted.

The first two MVCO deployments (winter, 2001-2002 and winter, 2002-2003) were conducted with a single optically instrumented mine placed within the field of view of a sidescan sonar. The mines were placed in fine and coarse sand, respectively. The third deployment late in 2003 consisted of 16 mines of various instrumentation and shape placed on both coarse and fine sand along with both sidescan and pencil beam sonar systems and multibeam bathymetric surveys. These mines were later repositioned for the fourth deployment and recovered in April, 2004 (Traykovski et al. 2006). All mines were deployed in approximately 12 m water depth about 1.5 km offshore.

Scour pits were seen to rapidly form in fine sand during the first storm event during each individual deployment, sinking and burying the mine such that between 40-80% of the mine was buried. Subsequent storms enlarge the scour pit to a point at which the mine approximately level with, or slightly below the ambient seafloor. Infilling by mud occurs during calm periods between storm events until the infilled mud can support fine sand, covering the scour pit and mine to a depth of about 10 cm. Coarse sand deployments showed that mines never completely bury in larger diameter sands. Rather, they sink and bury to a point where they present the same hydrodynamic roughness as the surrounding sand ripples supported by the coarse sediment (Traykovski et al. 2006). Work detailed here within pertains to an instrumented mine placed in fine sand within

the field of view of a pencil beam sonar during the third deployment at the Martha's Vineyard Coastal Observatory.

1.3 Chapter Preview

Experimental data from an instrumented mine in fine sand during the third Martha's Vineyard Coastal Observatory deployment and data correction techniques for a rotary pencil beam sonar are presented in the following chapters. Chapter two discusses the deployment site at the Martha's Vineyard Coastal Observatory, specific instruments deployed, and the oceanographic conditions during the deployment. Chapter three examines error introduced into the experiment through the pencil beam sonar, and methods to extract and correct the error in post data collection processing. Chapter four explores scour pit dimensions measured after all applicable correction algorithms have been applied, and gives some burial results relative to both the scour pit depth and mine diameter exposure above the far field ambient seafloor. Chapter five contains a look at scour pit progression during storms, summarizing the scour-infill-bury process as it relates to wave heights, hydrodynamic forcing, and bed-load transport.

2. DEPLOYMENT DESCRIPTION

2.1 Martha's Vineyard Coastal Observatory

The Martha's Vineyard Coastal Observatory (MVCO) was built by the Woods Hole Oceanographic Institute (WHOI) near South Beach in Edgartown, Massachusetts, and first became operational in June 2001 (figure 2.1). The MVCO contains a small shore lab with a meteorological mast, an offshore air-sea interaction tower, and a subsurface node mounted in 12 meters water depth approximately 1.5 kilometers offshore. This subsurface node contains electrical components that can power instruments and telemeter data to the MVCO shore lab via an embedded electro-optical power cable, which is then transmitted to WHOI via a T-1 data line (Austin et al. 2002). The 12-m node was instrumental in data collection, as the ability to communicate with a two-axis rotary pencil beam sonar (to be discussed later) connected to the 12-m node allowed for necessary sonar range changes to be made.

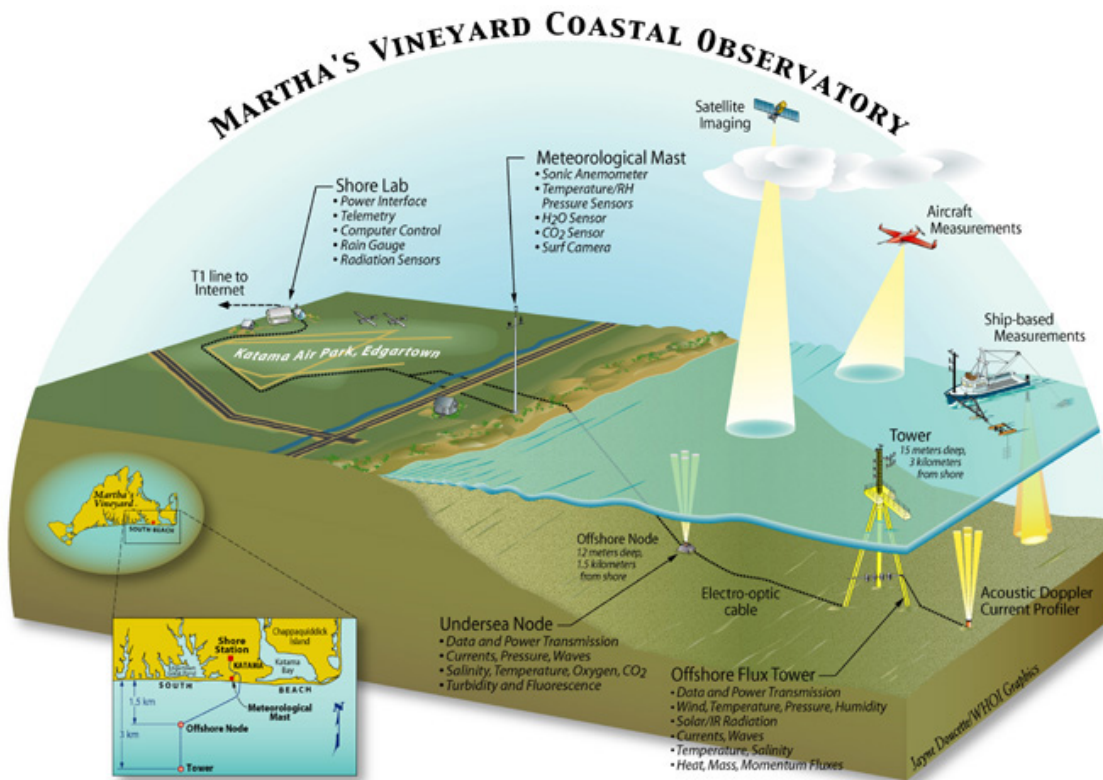


Fig 2.1
Schematic of the Martha's Vineyard Coastal Observatory,
showing land-based, sea-based, and airborne components
with available instruments and measurements. (MVCO
website, <http://mvco.whoi.edu/cgi-bin/mvco/mvco.cgi>).

The 12-m seafloor node is equipped with a variety of sensors, several of which were used in analysis of the oceanographic conditions during the mine deployment. A RD Instruments Workhorse 1200 kHz Acoustic Doppler Current Profiler (ADCP) was used to provide velocity profiles and directional wave spectra, a Paroscientific high-resolution pressure sensor provided tidal and wave information, and a YSI 6600 oceanographic sensor suite was on site to provide water property measurements (Austin et al. 2002).

2.2 Instruments Used

2.2.1 Acoustic Instrumented Mine

Several instruments were deployed from 30 September 2003 until 5 December 2003 to collect *in situ* data to assess mine scour and burial properties. Primarily, an Acoustically Instrumented Mine (AIM), developed and built by Omni Technologies Inc. and the Naval Research Laboratory, based on a previous design by the German firm Forschungsanstalt der Bundeswehr für Wassershall und Geophysik was used as a model mine. The AIM is an improvement over model mines used in two previous deployments during the winters of 2001-2002 and 2002-2003, where Optically Instrumented Mines (OIM) were used (figure 2.2). The primary motivation for developing a new model mine was two-fold. The OIM had 72 point optical sensors, used for measuring the state of mine burial. The optical sensors projected beyond the hull, hydrodynamically affecting the boundary layer water flow around the mine, possible enhancing burial. Marine growth and biofouling on the sensors limited the effectiveness and reliability of this method over the extent of the deployment. (Traykovski et al. 2006; Griffin et al. 2003).

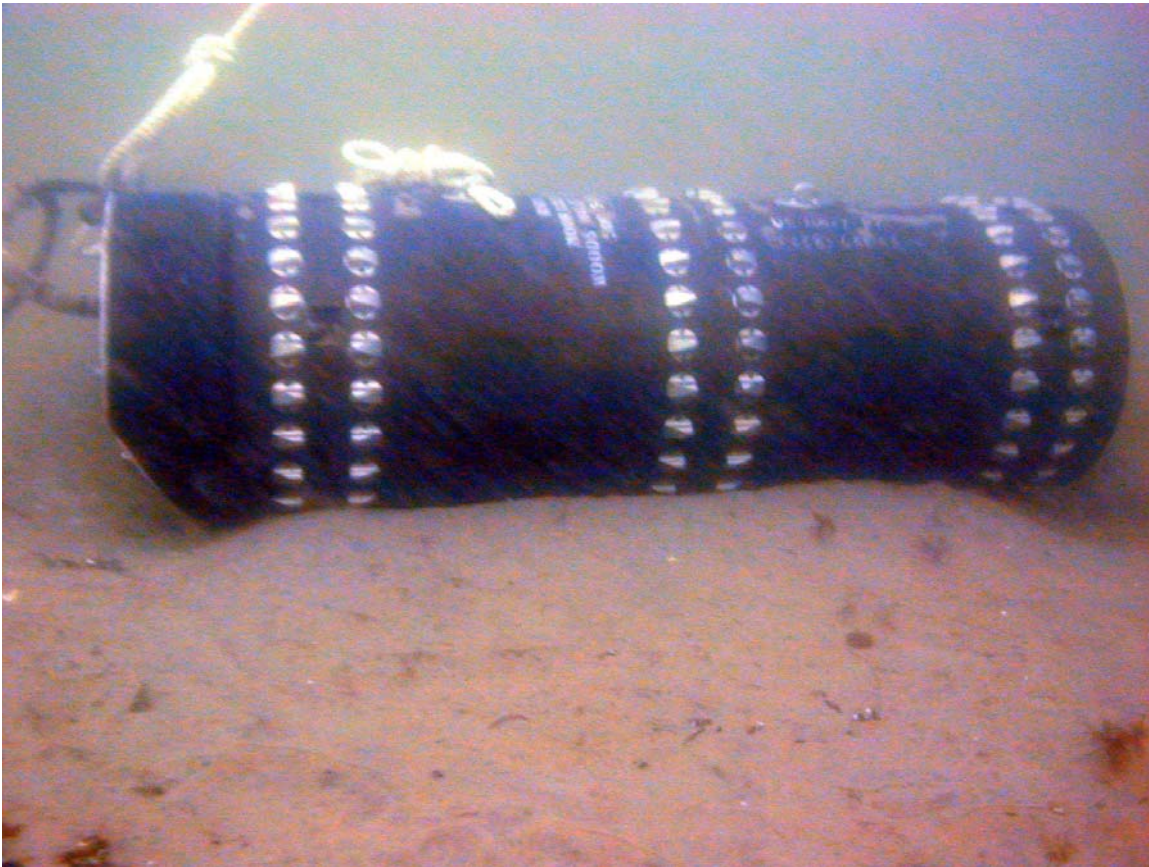


Figure 2.2
Optically Instrumented Mine (OIM) deployed at the Martha's Vineyard Coastal Observatory. The protruding optical sensor transmitter/receiver pairs are clearly visible beyond the hull of the mine. (Photograph by Richard I. Ray, NRL).

The AIM used for this deployment replaced the 72 optical sensors with 112 acoustic burial sensors (fig 2.3). The acoustic transducers were mounted flush with the hull of the mine, eliminating the negative effects associated with the optical sensors. All mine instrumentation was contained within a cylindrical naval marine bronze housing. The housing is 2.033 meters in length with a diameter of 0.533 meters. On board instrumentation included 6 pressure sensors, three solid-state compasses, and a three-axes accelerometer, giving a full load weight

of 900 kg (in air), and average density of 1984 kg/m^3 (Traykovski et al. 2006; Griffin et al. 2003).



Figure 2.3
Acoustically Instrumented Mine (AIM) ready for deployment. Acoustic transducers, while visible, are seen to be flush with the hull of the mine (Photograph from OTI website, <http://www.otiengineering.com/MineData/>).

The acoustic sensors operated at 1.5 and 3 MHz frequencies, and were evenly distributed around the surface of the mine, with 10 circumferential rings of 10 sensors spaced evenly along the length of the cylinder, and 6 sensors at each end. Sensors in each adjacent ring are offset by 18° from each other. Similar to the OIM, the sensors were again used to determine surface burial state at each transducer location, but the different geometry reduced many of the problems

associated with the previously used optical method. Also, analysis of the radial distance from each transducer to the sediment-water interface allowed for a first order approximation of the scour pit dimensions. The transducer elements were recessed 2.5 cm inside the hull surface, set in urethane. Urethane is acoustically transparent in seawater, and the offset provided the necessary range to eliminate interference between transmitted and reflected signals, allowing for measurements of sediment directly on the transducer face. However, large suspended sediment concentrations during storm events can cause false returns (Griffin et al. 2003).

Six diaphragm style pressure sensors were used to monitor wave conditions and changes in mean water depth. They were mounted at 60° intervals around the circumference of the mine, and had a range of 0 to 100 psi giving a maximum water depth of approximately 45 m with a sensitivity of about 1 mm. Measurements were made at a sample interval of 71 minutes, 45 seconds. Stainless steel filters covered the sensor diaphragm to reduce damage to the sensor (Griffin et al. 2003). The 6 onboard pressure sensors were used to calculate tidal heights and wave statistics. The MVCO 12-m node provided a fixed pressure sensor measurement. Comparison between the MVCO and AIM pressure sensors allowed for relative mine elevation change estimations. Ultimately, the MVCO pressure measurements were used for determining wave statistics, due to the close proximity to ADCP water velocity measurement locations.

The orientation measurements were made with three standard off-the-shelf solid-state compasses and a three-axes accelerometer. Heading measurements were accurate to $\pm 2.0^\circ$ and pitch and roll measurements were accurate to $\pm 0.5^\circ$. The accelerometer had a range of $\pm 39.2 \text{ m/s}^2$ (4 G's), and a sensitivity of 0.98 m/s^2 (0.1 G) (Griffin et al. 2003). Both instruments had a 15 minute sample time. These measurements were used to confirm mine orientation changes measured by sonar imaging techniques.

2.2.2 Rotary 2-Axis Pencil Beam Sonar

While the AIM contains several different instruments useful in measuring the local bedform characteristics, wave climate, and mine orientation, these measurements were all in support of the principal means of documenting mine scour and burial. The most widely used source of data in this thesis came from an Imagenex pencil beam sonar, capable of producing quantitative microbathymetric measurements with centimeter scale resolutions.

The sonar system had an adjustable center acoustic frequency set to 975 kHz with a $10 \mu\text{s}$ pulse length and approximately 2.5° beamwidth. The maximum range sampled was 5 m. The sonar was mounted on a 2 in diameter 4 m length pole approximately 2 m above the ambient seafloor, with the remaining length water-jetted into the seafloor about 2.5 m from the center of the mine (Traykovski et al. 2006). Also mounted on the pole was a rotary sidescan sonar. Data from both systems was transmitted to land via the 12-m node, which allowed for the

sonar range to be necessarily adjusted during the deployment (Richardson and Traykovski 2002). Unfortunately, the sonar range was set too short for the first 7 days of deployment, and consequently only about half of the mine was resolved, however, accelerometer and compass data can be used to eliminate mine movement during this period. The total drag of both sonar systems on the pole proved troublesome, as storm events forced the pole to tilt from vertical, shifting the geographic origin of the pencil beam coordinate system during the deployment. Steps were taken to correct for this in post processing, which will be detailed later.

The pencil beam sonar was mounted with two stepper motors, allowing for rotation in two axes. Horizontally, the sonar head was rotated through 180° in 2.4° increment steps, giving 75 linear slices. Additionally, the sonar was vertically rotated through 180° in 1.2° increment steps, resulting in 150 recorded points along each slice. Combined, these two rotational parameters allowed the sonar to image an entire hemisphere below the transducer. This geometrical setup affected the resolution of the seafloor. The horizontal resolution is highest directly under the transducer and decreases with radial distance away from the sonar head, with an approximately 10 cm resolution at the mine's location. Pencil beam sonar images were made with a sample period of 1 hour (Traykovski et al. 2006). Ground faults in the 12-m node power system as well as large suspended sediment concentrations and water velocities during storm events resulted in a random distribution of bad sonar images, and thus mine

scour and burial was not analyzed with the hourly sample time for the entire deployment.

Post data collection, a threshold detector on the leading edge of the returned signal was used to determine range from the sonar transducer to the seafloor. Backscatter data has been range corrected for spherical spreading and attenuation with the system's time variable gain (Traykovski et al. 2006). The returned seafloor was also corrected for differences between the exact position where the leading edge of the sonar pulse encountered the seafloor and where the center of the transducer was pointed, based on the grazing angle with the local seafloor. The primary motivation for this was that the finite beam pattern of the sonar combined with the thresholding method produced geometric distortion of the seafloor microtopography. This correction method will be thoroughly described in chapter 3.

2.2.3 Additional Mine Deployment

Several other mines were deployed at the same time as the AIM used in this experiment. In total, 4 AIMS and 6 OIM's were deployed, along with six inert non-cylindrical shapes (fig 2.4). The inert shapes had no internal instrumentation, and were used to visually determine the long term burial characteristics of mines with varied geometries through the use of scientific divers (Richardson and Traykovski 2002; Traykovski et al. 2004).

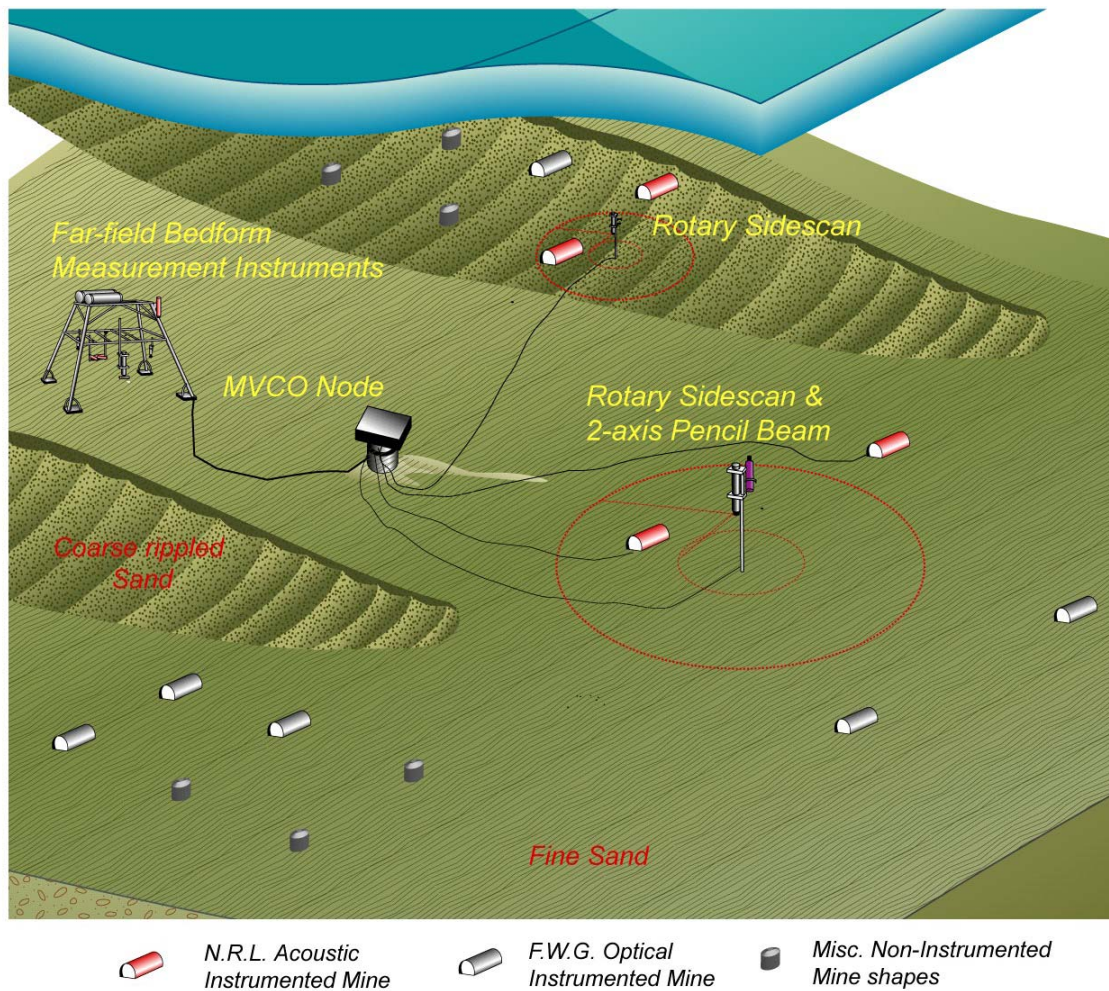


Figure 2.4
Schematic of the Martha's Vineyard Coastal Observatory 12-m node deployment area showing the layout of acoustically and optically instrumented mines, as well as inert shapes, in different types of sand. (Traykovski et al. 2004).

Mines were deployed in three groups around the 12-m node to take advantage of the varying bedform features in order to characterize mine scour and burial in both fine and coarse sand. A minimum of 25 m spacing between mines was sought to prevent scour pits from adjacent mines influencing each other. In addition to the mine described in this experiment, a second AIM was

also deployed in fine sand without any imaging sonars, and two others were placed in coarse sand, one with a single rotary sidescan sonar and one without any imaging sonars. Some mines were placed perpendicular to the dominant wave direction for the region, as well as parallel to the local ripple crests, while others were parallel to the dominant wave direction. At the end of the initial deployment, from which data is contained here within, all mines were located and repositioned, remaining in the water until 18 April 2004.

2.3 Environmental Conditions

2.3.1 Oceanographic Conditions

Situated on the south coast of Martha's Vineyard, the MVCO is sheltered to the north by the island of Martha's Vineyard, as well as to the east by shallow waters at Wasque Shoals, resulting in waves originating predominantly from southerly directions. Typical of the Atlantic Basin, wave heights are largest in the winter from October to March, coinciding with the deployment period (Traykovski et al. 2006; Richardson and Traykovski 2002; Traykovski et al. 2004). The largest significant wave heights measured by the Paroscientific Pressure Sensor at the 12-m node since the MVCO first became operational in June 2001 to present were observed to be between 3 and 4 m with peak wave periods of 8 to 13 seconds associated with the largest wave events. The maximum wave height was measured to be 4.1 m in late December 2003 (fig 2.5).

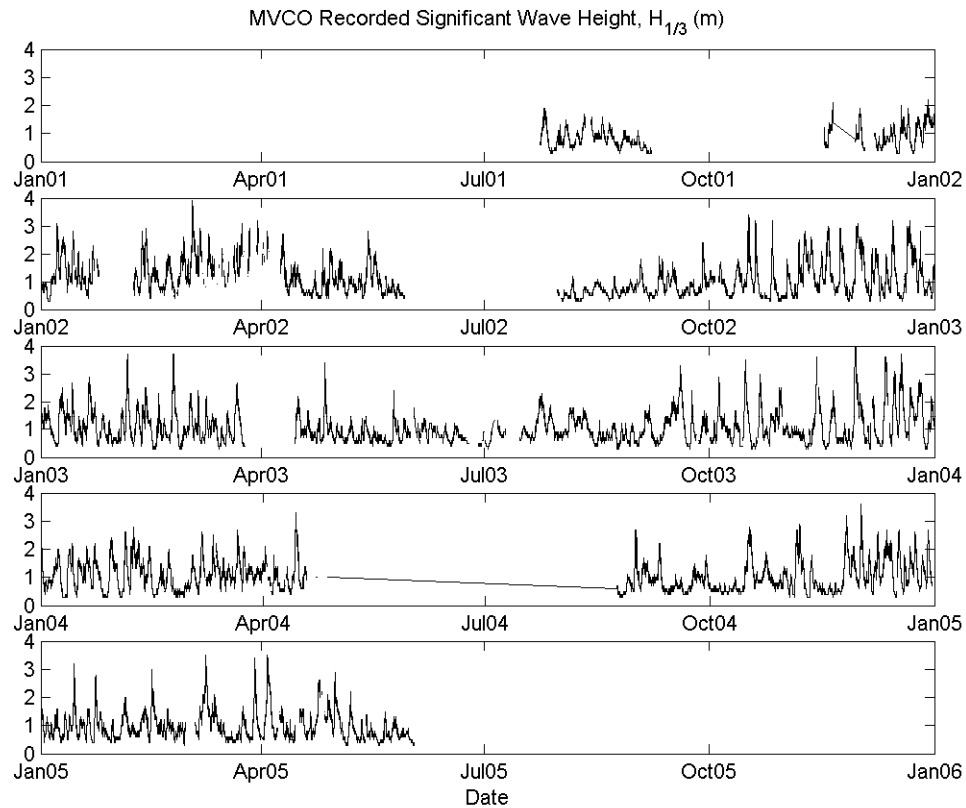


Figure 2.5
Significant wave height history ($H_{1/3}$) at the Martha's Vineyard Coastal Observatory 12-m node, measured by the on-site Paroscientific Pressure Sensor. Wave heights, in meters, are shown from when the MVCO first became operational in the summer of 2001 until present. Gaps in wave height are primarily due to ground faults at the MVCO.

There were 8 storm events with significant wave heights greater than 2 m during the actual deployment of the mine from 30 September to 5 December 2004 (fig 2.6).

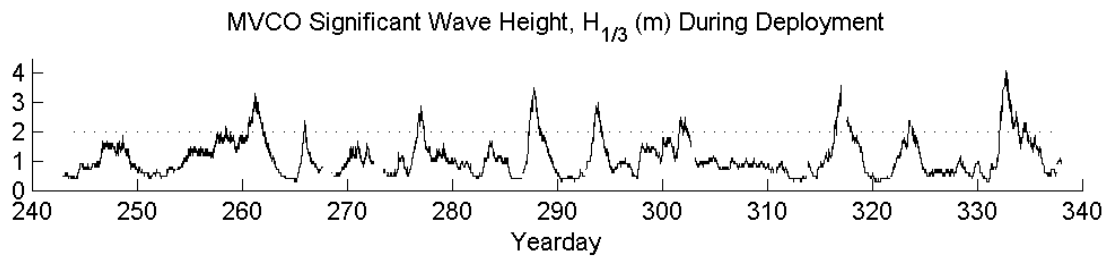


Figure 2.6
Significant wave heights ($H_{1/3}$) at the Martha's Vineyard Coastal Observatory 12-m node during mine deployment, measured by the on-site Paroscientific Pressure Sensor. Heights are shown in meters. Year day 0.5 is 1200 EST, 01 January. Heights above 2 meters (shown here by a dotted line) are classified as large storm events.

The most significant scour and burial changes occurred during and immediately following these storms. This was visually observed from the 2 axis pencil beam sonar images and was confirmed with solid-state compass pitch and roll data.

Near bottom water velocities were also measured at the 12-m node by the RDI ADCP. Wave generated orbital velocities reached r.m.s values of 50-70 cm/s during the 8 large storm events (fig 2.7). Tidal induced bottom currents were typically around 10-20 cm/s, with combined wind and tidal velocities in the 30-40 cm/s range (Traykovski et al. 2006; Richardson and Traykovski 2002; Traykovski et al. 2004). Wave generated velocities, with their larger associated shear stress relative to mean currents with similar velocities, were the major forcing factor in mine scour and sediment suspension (Grant and Madsen 1979).

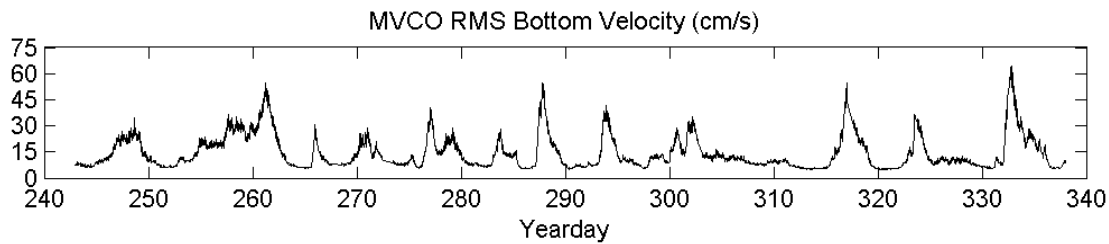


Figure 2.7
Root-mean-square Bottom Velocity (URMS) at the Martha's Vineyard Coastal Observatory during the mine deployment measured by the on-site RDI ADCP. Velocities are shown in cm/s. Year day 0.5 is 1200 EST, 01 January.

2.3.2 Seabed Characteristics – Large and Small Scale Bedforms

The bathymetric characteristics around the MVCO and the 12-m node have been surveyed in great detail, and much is written about it (Goff et al. 2005). A short summary description is included here. Fingers of coarse sand sorted bedforms extend perpendicular from shore for several kilometers (fig 2.4). They range in width from 100's to 1000's of meters wide. The coarse sand has a mean grain size of 0.50 to 1.00 mm. Fine sand, where the mine was placed, inhabits the region between the coarse sand fingers with a mean grain size of 150 to 180 μm . The local seabed in these fine sand regions is stratified by depth, with a top fine sand region, followed by a transitional gravel layer, then an underlying coarse sand layer. The gravel layer was also seen in the coarse sand regions, at typical depths of 10 to 50 cm (Traykovski et al. 2006; Traykovski et al. 2004).

Grab samples and seismic profiles were employed to describe the sediment in the immediate deployment area. The sediment in the vicinity of the deployment site is characterized by fine quartz sand with a mean grain size of 0.18 mm, average grain density of 2661 kg/m³, porosity of 38.5%, and bulk density of 2042 kg/m³. By weight, an average of 95% of the grains were sand-sized with most grains between 0.1 and 0.3 mm (Richardson and Traykovski 2002).

In the fine sand, small ripples with wavelengths of 10 to 20 cm and heights of 1 to 2 cm were seen in a rotary sidescan sonar imagery of the site. These ripples were washed out during large wave events. Also present were larger bedforms in the fine sand, with lengths of 3 to 5 m and heights of 10 to 15 cm (Traykovski et al. 2006; Traykovski et al. 2004). As will be discussed later, the scour pit and mine were later covered with fine sand and mud. These bedforms may be the source of the fine sand and mud covering the scour pit.

3. DATA SET POST PROCESSING CORRECTIONS

3.1 Beam Pointing Corrections

3.1.1 Motivation for Corrections

Ideally, the sonar signal produced by the pencil beam sonar would have an infinitesimally small beam width. In practice, the Imagenex sonar used has a 2 to 3 degree beam width. For some purposes, the approximation of an infinitesimally narrow beam is acceptable. To obtain the level of resolution needed to make the qualitative measurements necessary for analysis of mine scour and burial characteristics in this experiment, this approximation causes some problems.

Most obvious is the distortion of the mine. Any heavy object placed into fine sand will not sit entirely on top of the seafloor. Several methods can cause this. Either initial seafloor scour will cause the object to sink directly into the seafloor, or some slight burial will be exhibited directly at impact. Also, the extreme top layer will be at least partially liquefied, and the weight of the object will compress this layer directly beneath it, causing the object to sink to some extent relative to the seafloor surrounding the object. The density of the mine is approximately 3 times the seafloor density (1.9 kg/m^3 versus 0.65 kg/m^3), and thus the mine will definitely sink relative to the surrounding seafloor if the seafloor consists of mobile sediment. This causes a significant portion of the 53.3 cm

diameter to be covered by sand and thus lost via sonar imaging techniques. Assuming a narrow beam, the uncorrected system produced mine heights of approximately 53 cm relative to the bottom of the scour pit which it was in.

This error is derived from the angular difference between the center of the beam width and the point of shortest range to the seafloor within the beam width (fig 3.1).

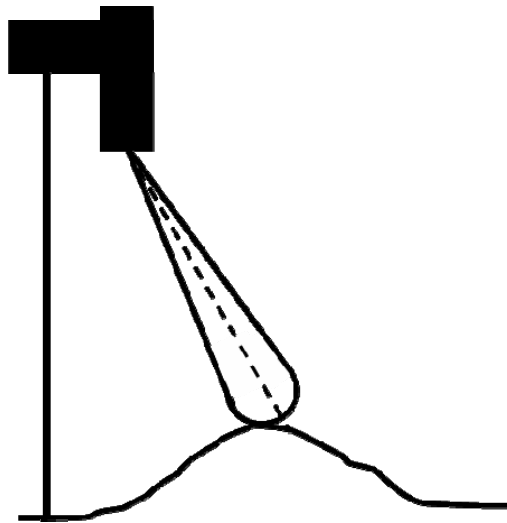


Figure 3.1
Schematic of the difference between the point where the sonar is aimed (dashed line) and the closest point within the beam width to the transducer face.

As seen above in figure 3.1, the range to the point on the seafloor being measured will be correct. It is a simple calculation converting acoustic travel time to the point and back into distance. The error will be introduced into the system when the range is mapped into a point in the sonar coordinate system.

The point closest to the sonar (i.e. shortest range) within ± 1.25 degrees (i.e. half the beam width) of the direction that the transducer face is aimed will be the first reflection to arrive at the transducer in the returned signal, and thus will be the only return to pass the leading edge threshold. Regardless of where this point is in the beam width, it will map as if the point originated from the direction of the center of the beam width where the sonar was aimed. Mapping to this location will change both the radial distance from the base of the pole, as well as the vertical distance below the sonar. In the above diagram in figure 3.1 this results in the measured “bump” being farther away from the base of the sonar pole and higher off the ambient seafloor, exactly what was happening in the mine deployment. The errors derived from beam pointing effect in both theoretical and actual sonar data can be seen below (fig 3.2).

As seen in the theoretical case below in figure 3.2, the mine is originally mapped well above the actual mine. In practice, the mine is being imaged with a height of approximately 53 cm relative to the bottom of the scour pit which it is sitting in. While 53 cm is the actual diameter of the mine, some of the mine is embedded in the seafloor, thus the measured height should be lower.. As mentioned in section 3.1.1, a portion of the mine’s diameter will be covered with sand as the weight of the mine causes it to sink into the seafloor, and thus lost via sonar imaging techniques. Consequently, the sonar is returning a larger mine than actually exists due to beam pointing errors.

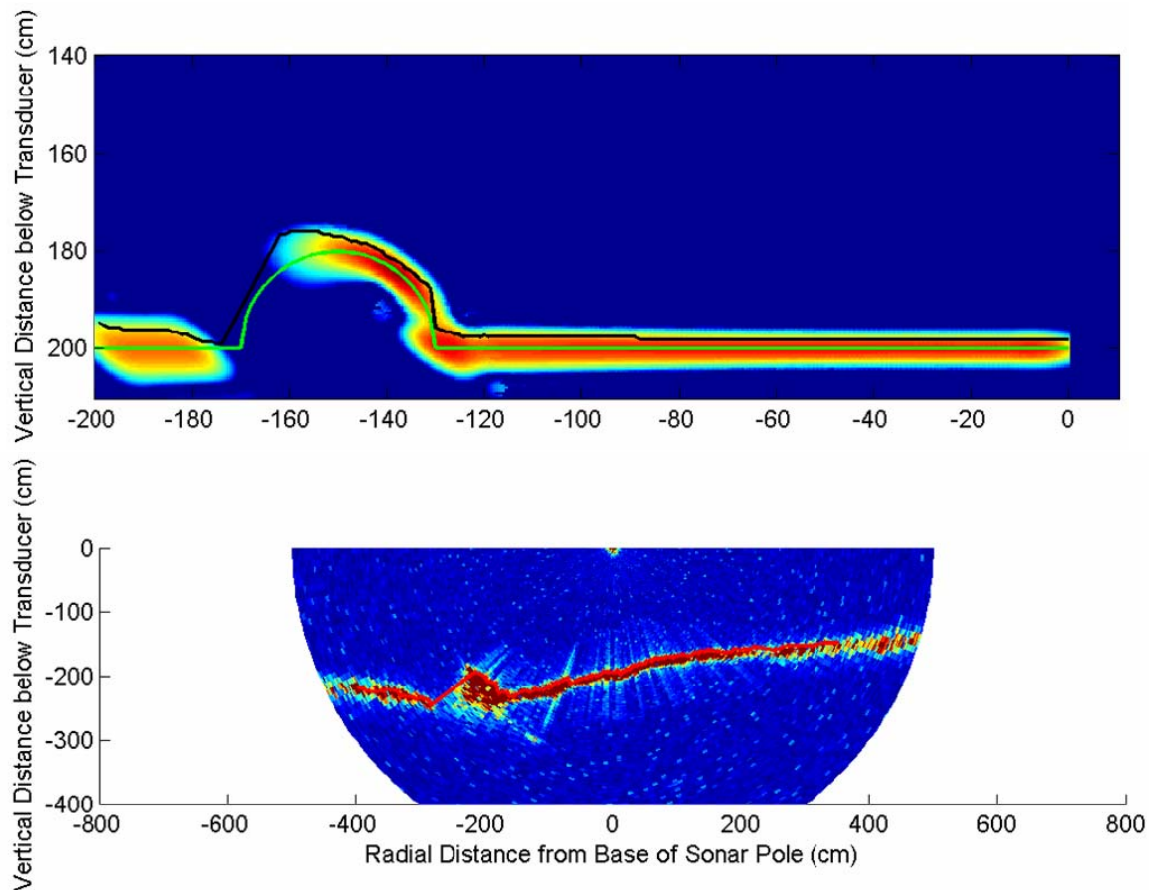


Figure 3.2

The top plot shows the theoretical difference between actual (green) and mapped (black) seafloor points due to beam pointing errors. The bottom plot shows the mapped seafloor (red line) versus range from the sonar transducer for one slice with the 2 axis pencil beam sonar. The height of the mine (large bump) is approximately 53 cm. Both plots are overlaid on an un-calibrated log scale intensity, represented by color.

The theoretical plot was created by first finding the acoustic backscatter intensity returned from the model surface, defined by a half circle of diameter 40 cm flush with a level ambient seafloor (green line in figure 3.2). The acoustic intensity is defined as:

$$I(r, \theta) = \int \frac{B(\theta - \theta')}{r^2} \delta(r - r_s, \theta - \theta_s) d\theta' dr \quad (1)$$

where I is the acoustic backscatter intensity, θ is the central angle of the beam pattern (transducer steering angle), θ' is the angle from the beam pattern central angle to the point within the beam pattern, θ_s is the angle from the transducer to the seafloor point, r is the range from the sonar, r_s is the range from the sonar to the seafloor point, and B is the beam pattern,. The beam pattern in this case is a sinc function limited to the main lobe, where the main lobe has a width of 2.5° , to be consistent with the physical characteristics of the 2-axis pencil beam sonar (figure 3.3). The returned surface is defined as the point where the backscatter intensity reaches 70% of the maximum returned backscatter intensity for each acoustic ping. This is similar to the threshold detection method described in section 2.2.2.

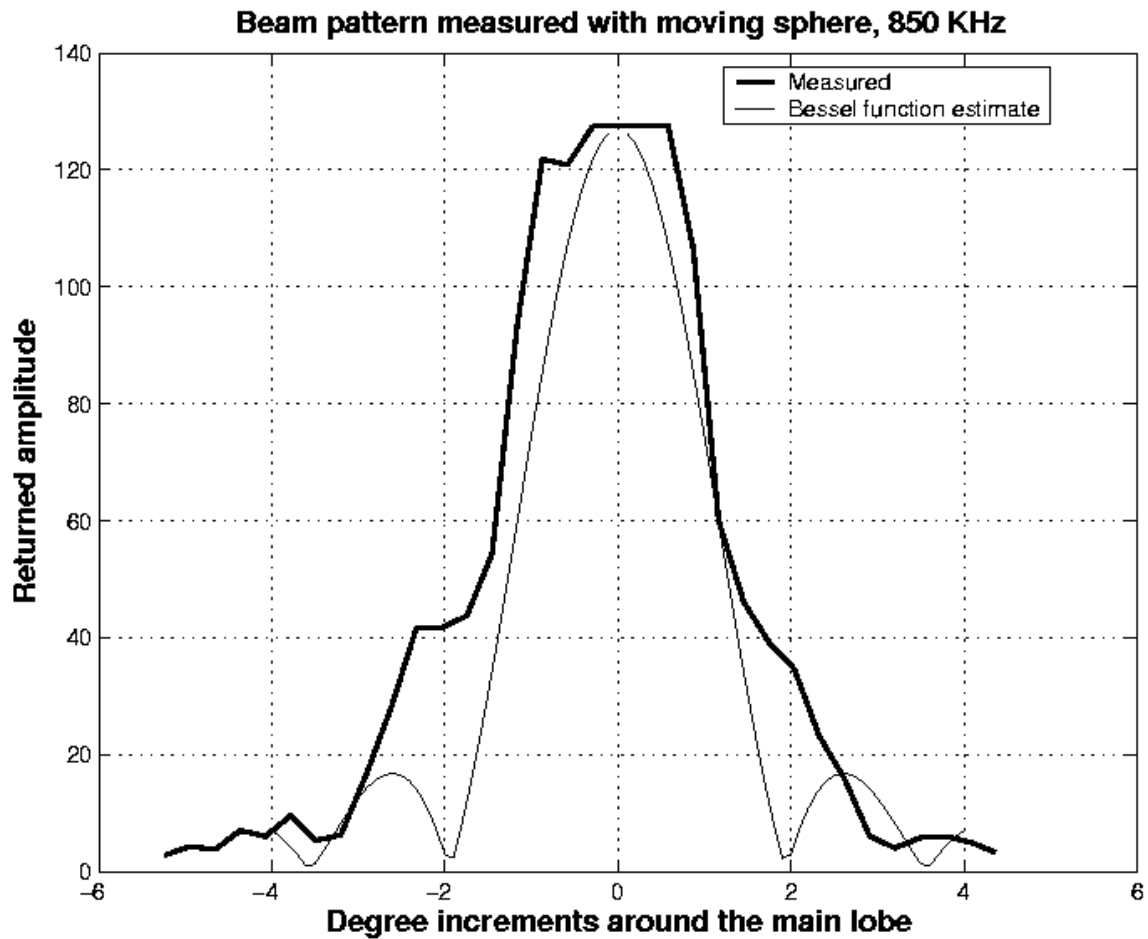


Figure 3.3
Plot of returned (thick line) and estimated (thin line) acoustic backscatter intensity for the 2-axis pencil beam sonar beam pattern. The estimated beam pattern was found from a Bessel function estimate.

3.1.2 Geometric Correction Technique

Corrections for the distortion explained in section 3.2.1 were made based on the angle of the direct-path line to the mapped seafloor point with the local seafloor normal (α). This is a simple geometric process (fig 3.4). First, the local slope of the seafloor (S) had to be found. The local slope was defined to be the

average of the slopes between the point of interest and neighboring points radially closer and farther away from the base of the sonar pole. At the extreme outside edge of the sonar range the slope was simply between the two farthest points from the base of the pole.

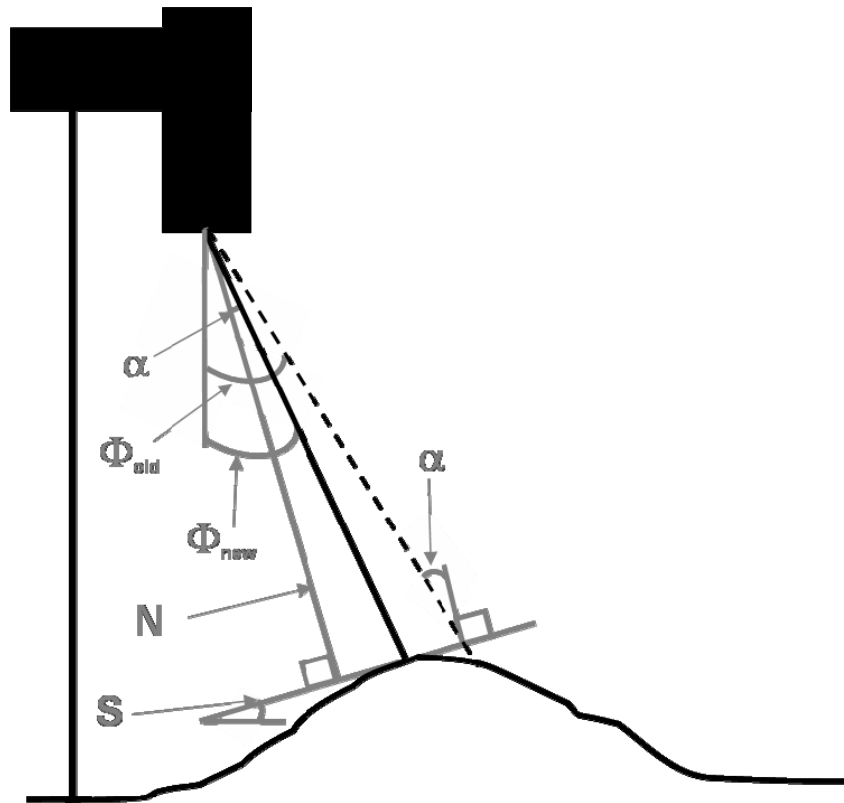


Figure 3.4
Schematic describing the trigonometry required to solve for Φ_{new} , the angle between the direct-path line to the closest point with in the seafloor and vertical. Trigonometric features are shown in gray.

After the local slope was found, the normal to that surface (N) was then found. The normal is simply the slope plus 90 degrees (figure 3.5).

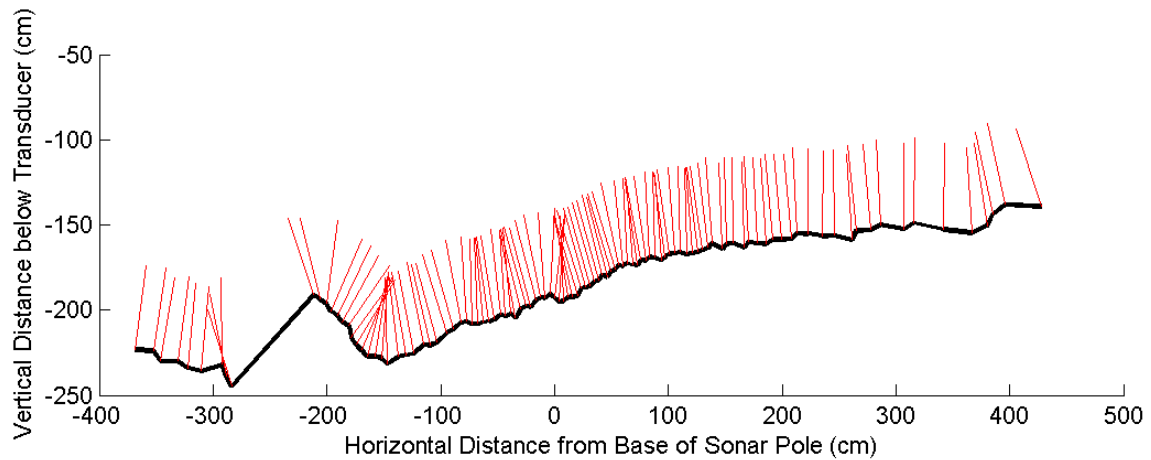


Figure 3.5
Plot of surface normals, N (red), found from the local seafloor slope, S (black). Normals have been adjusted in magnitude for better viewing.

After this, the normal was used to find the angle between the local seafloor normal and the center of the beam width, the direction in which the transducer face was pointed (figure 3.6).

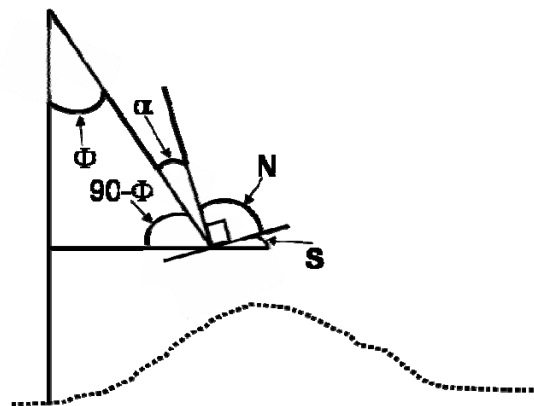


Figure 3.6
Schematic showing how α , the angle between the center of the beam width and the normal to the local seafloor slope is found from Φ_{old} and S.

The angle between the direction of the transducer face (Φ_{old}) and the seafloor normal (N) was calculated as:

$$\alpha = 180 - (90 - \phi) - N = \phi - S \quad (2)$$

where α is the angle between the local seafloor normal and the center of the beam width and between the N is equal to $S + 90$. Once α was found, a simple algorithm was followed to compare it with the beam width and to adjust the original mapping angle (Φ_{old}). This algorithm is described below:

$$\begin{aligned} &\text{If } -BW/2 \leq \alpha \leq BW/2 \\ &\quad \text{Then } \Phi_{new} = \Phi_{old} - \alpha \\ &\text{If } \alpha < -BW/2 \text{ or } \alpha > BW/2 \\ &\quad \text{Then } \Phi_{new} = \Phi_{old} - (BW/2 * \text{sign}(\alpha)) \end{aligned}$$

If α lies within the beam width of the pencil beam sonar, then the new mapping angle (Φ_{new}) will be at this angle off the central direction of the transducer, while retaining the original range. If α is larger than the beam width, then the new mapping angle adjusted to lie on either the inside or outside edge of the beam, the closest possible angle to the measured seafloor point, and is mapped with this angle at the original range.

These corrections were only made in the radial direction. This is because the spacing between radially neighboring points is much smaller than neighboring points with the same radial distance, but on different sonar slices. The stepper

motors stepped in 1.2 degree increments through each slice. At the mine's location approximately 2.25 meters from the base of the sonar mounting pole, this equates to roughly 4.7 cm spacing between points, versus 9.4 cm spacing between horizontally adjacent points with a 2.4 degree incremental step between each slice. The small, fine-sand ripple wavelength in the deployment area is approximately 10-20 cm (discussed in chapter 2). Thus 10 cm spacing between points is large enough for local variations in the seafloor to cause the employed method of determining the local slope to break down.

Employing this correction yields a mapped mine height that is consistent with a partially buried 53.3 cm diameter mine. The result is shown below for the same slice as in figure 3.2 (fig 3.7). Beam pointing error corrections reduce the mine height relative to the surrounding seafloor from 53 cm to approximately 47 cm. A secondary effect of this correction is to remove the “doming” of a flat seafloor, and also flatten out the high frequency fluctuations in the ambient seafloor away from the scour pit, eliminating the need for some of the final noise reducing filtering.

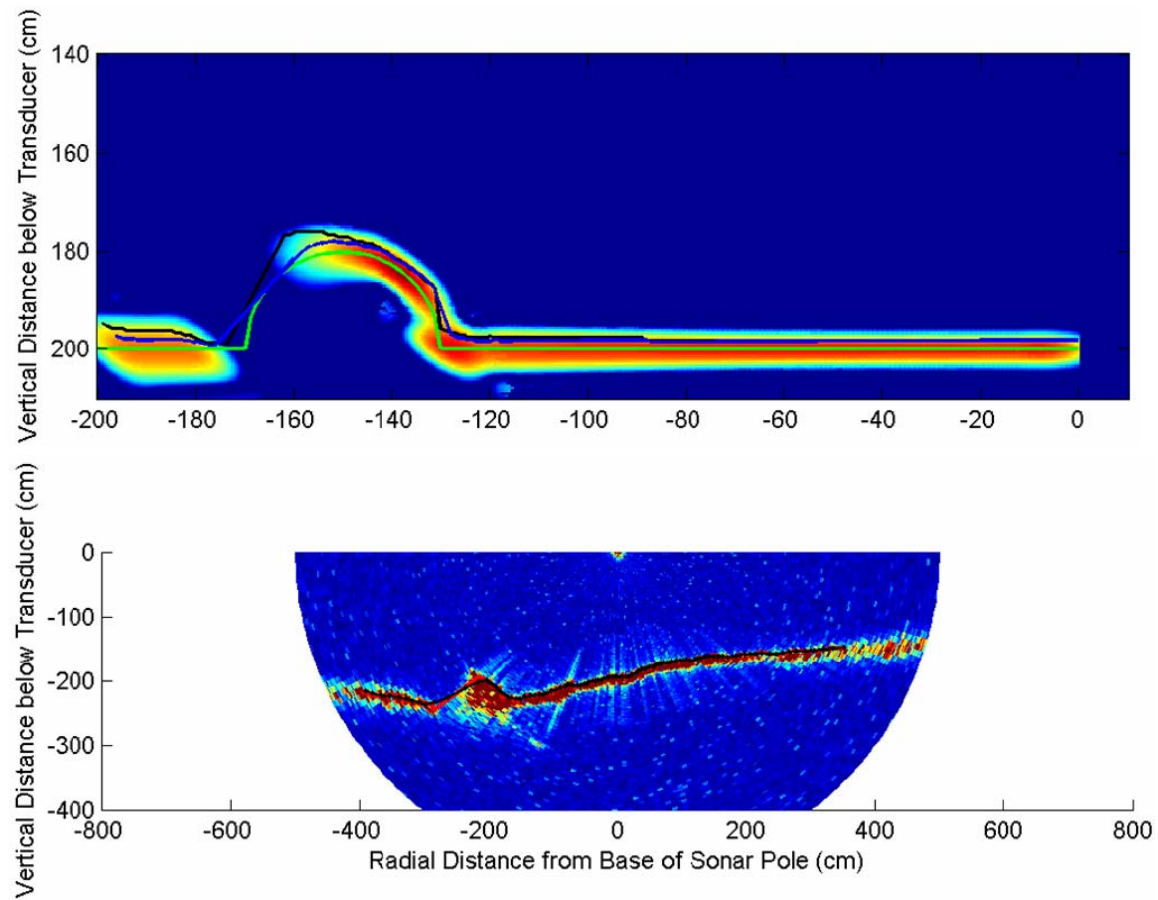


Figure 3.7

The top plot shows the uncorrected surface (black) and corrections (blue) to a 40 cm diameter model mine flush with a flat seafloor (green). The bottom plot shows the original (red) and corrected (black) mapped seafloor versus range from the sonar transducer for one slice of the 2 axis pencil beam sonar. Beam pointing corrections give a new mine height of approximately 47 cm relative to the surrounding seafloor. Both plots are overlaid on an uncalibrated log scale intensity, represented by color.

3.2 Pole Lean Corrections

3.2.1 Motivation for Corrections

The 2 axis pencil beam sonar was mounted at one end of a 4 m long pole, water-jetted approximately 2 m into the seafloor. This mounting method was chosen to project a smaller area compared to more traditional tripod mounting systems, minimizing the hydrodynamic effects of the mount on the seafloor and scour pit surrounding the mine from the mounting system. Due to sonar range limitations, the mine could not be placed far enough away from a tripod for the scour pit to be outside the wake zone of the tripod. Thus, a single pole system was employed.

As mentioned before in chapter 2, the seafloor where the mine was placed has a top layer of fine sand, a middle layer of gravel, and coarse sand underlying everything. This mounting system, while providing less outside influence, was not as stable in the fine sand at the deployment site as traditionally employed methods. Large wave events with their associated water velocities forced the pole to lean over from its original vertical position perpendicular to the seafloor, and rotate about the vertical axis (fig 3.8). The pole eventually fell over completely towards the end of the deployment. This changed the position of the sonar head, offsetting the origin of the coordinate system that the sonar was referencing its measurements from. The rotational lean of the pole from vertical caused the axes of the coordinate system to rotate away from their original

orthogonal settings. Spatially, the origin of the coordinate system was also shifted in three dimensions.

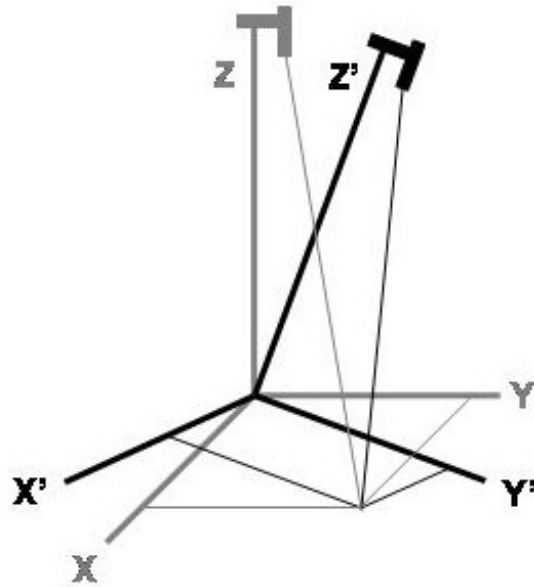


Figure 3.8
Schematic showing how the shifted coordinate system, due to lean and rotation of the sonar mounting pole, results in different Cartesian measurements to the same point. The gray (unprimed) axes are the original coordinate axes, and the black (primed) axes are the leaned and rotated axes.

This pole lean and rotation skewed the sonar measurements, as was clearly apparent when viewing the images (fig 3.9). The mine was placed in an area with little slope in the seafloor. However the original sonar images showed a large slope in the ambient seafloor in areas unaffected by the mine scour pit. There was no instrumentation available to measure the extent of lean of the mounting pole, and thus post processing methods had to be employed to correct the data sets.

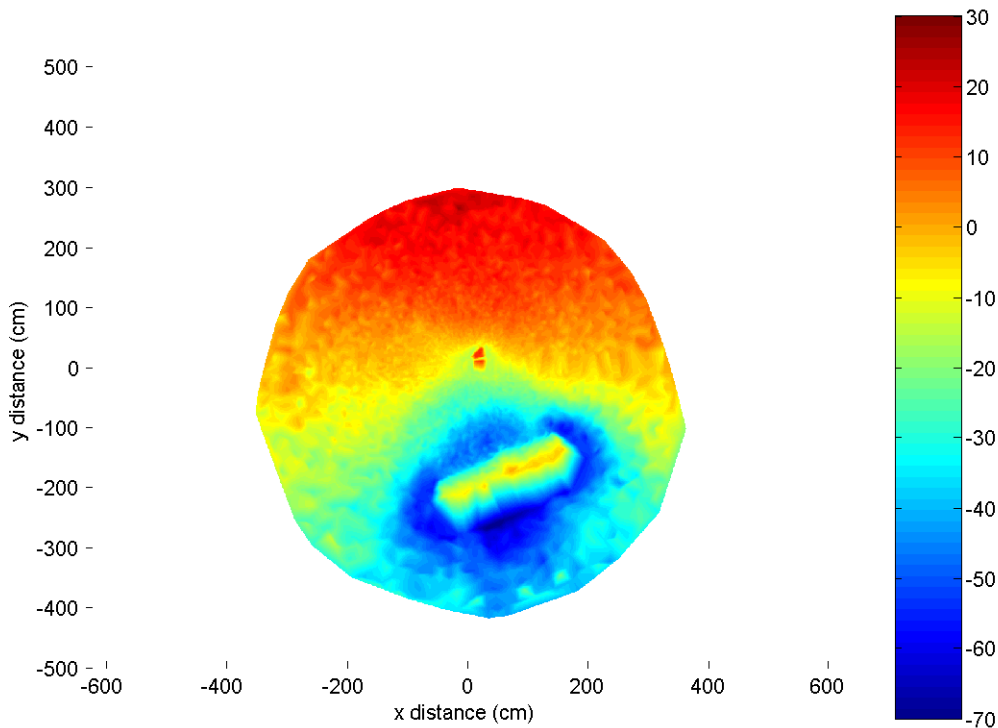


Figure 3.9
Image returned from sonar measurements affected by a
leaned and rotated pole mounting system. The color
represents vertical height, in cm, above the seafloor at the
base of the pole. Note the large, almost 1 meter, change in
elevation over the 7 meter distance from the top to the
bottom of the plot.

3.2.2 Correction Technique Theory

A three axis Cartesian coordinate system transfer function was used to correct the returned sonar images for the leaning mounting system. Specifically, a “1-2-3” transformation was used, where the X-axis was first rotated, followed by the Y-axis, and finally the Z-axis. This transformation method was chosen because the angle of pole lean away from the vertical axis (and the associated X-

and Y-axis rotation angles) was dominant over the minimal angular changes due to rotation of the pole around the Z-axis.

The transformation matrices are expressed as:

$$\begin{aligned} M_x &= \begin{bmatrix} 1 & 0 & 0 \\ 0 & C_x & S_x \\ 0 & -S_x & C_x \end{bmatrix} \\ M_y &= \begin{bmatrix} C_y & 0 & -S_y \\ 0 & 1 & 0 \\ S_y & 0 & C_y \end{bmatrix} \\ M_z &= \begin{bmatrix} C_z & S_z & 0 \\ -S_z & C_z & 0 \\ 0 & 0 & 1 \end{bmatrix} \end{aligned} \quad (3)$$

where M_x , M_y , and M_z are the individual transformation matrices for the X-, Y-, and -Z axes, respectively, S_x and C_x are the sine and cosine of the X-axis rotation angle, S_y and C_y are the sine and cosine of the Y-axis rotation angle, and S_z and C_z are the sine and cosine of the Z-axis rotation angle.

Combining the three individual transformation matrices by multiplying in the “1-2-3” order yields the overall transformation matrix, M :

$$M = M_x * M_y * M_z = \begin{bmatrix} C_y * C_z & C_y * S_z & -S_y \\ S_x * S_y * C_z - C_x * S_z & S_x * S_y * S_z + C_x * C_z & S_x * C_y \\ C_x * S_y * C_z + S_x * S_z & C_x * S_y * S_z - S_x * C_z & C_x * C_y \end{bmatrix} \quad (4)$$

Since the returned coordinates from the sonar are based on the rotated coordinate system, the goal is to transform the coordinates back to the original. This is expressed as:

$$X = \text{inv}(M) * X' \quad (5)$$

where X contains the transformed coordinates to eliminate changes caused by the leaning mounting pole, X' contains the coordinates originally returned by the sonar, and inv(M) is the inverse of the total transformation matrix, M.

3.2.3 Numerical Transformation Correction Technique

An iterative process was used to analytically determine the X, Y, and Z rotation angles. The processing was done after the sonar measurements had been corrected for beam pointing errors. Each rotational axis was allowed to vary through a range of angles in incremental steps of 0.05 degrees, allowing for all possible angular combinations. The standard deviation of a ring, 5 data points wide, encircling the outer edge of the sonar image was then calculated for each combination. The angular combination that resulted in minimum standard deviation was determined to be the correct rotational angles (fig 3.10).

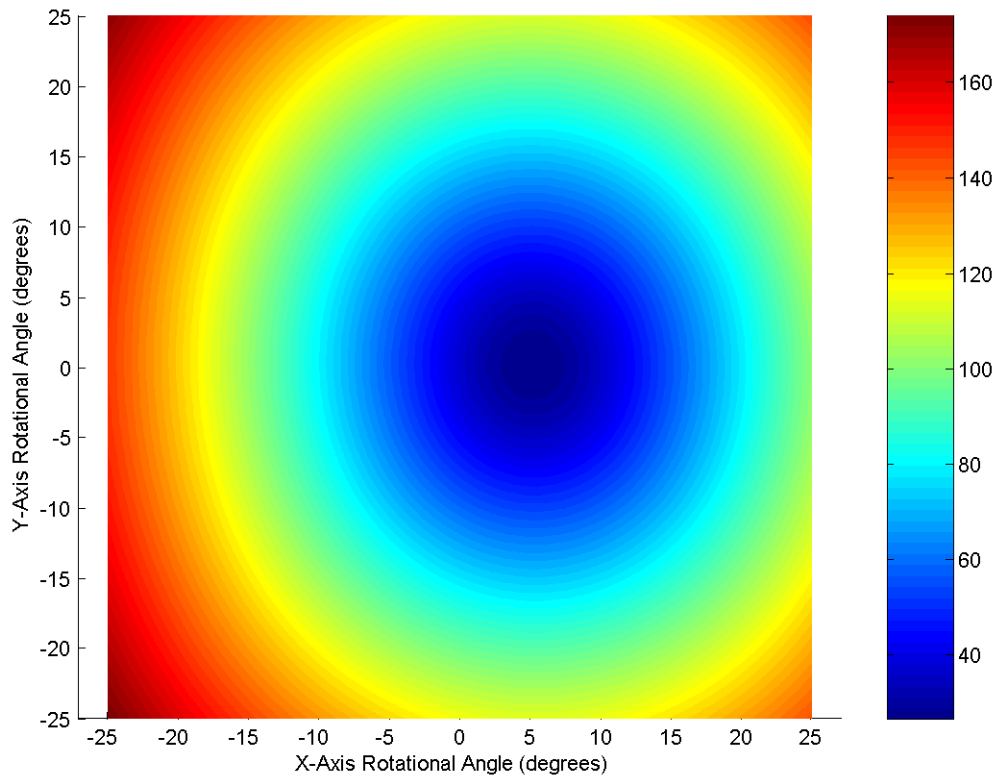


Figure 3.10
Plot of standard deviation (color) versus rotational transformation angles. There is a clear minimum (in this case at 5.15° and 0.1° for the X- and Y- axes rotational angles, respectively).

This technique was employed for all sonar images over the course of the initial mine deployment. The Z-axis rotational vector was extremely small throughout the entire deployment period (on the order of 0.2 degrees), and was thus ignored. Intuitively this makes sense, as it is a property of the “1-2-3” transformation method. In this method, the X-axis is first rotated and transformed about the original X-axis, creating new Y- and Z- axes. Then Y-axis is rotated and transformed about the new Y-axis created by the first X-axis transformation,

this time creating new X- and Z- axes. Finally the Z-axis is rotated and transformed about its newly created axis, which at this point has already been transformed twice. Consequently, the X-axis rotational angle will have the largest magnitude (approximately -7.3 degrees for this data set), followed by the Y-axis rotational angle (approximately 3.1 degrees for this data set), and Z-axis rotational angle will be the smallest (fig 3.11).

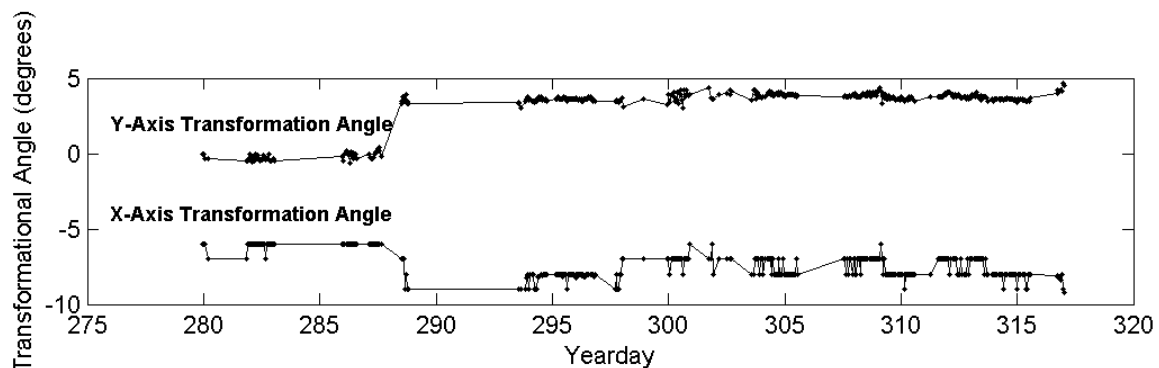


Figure 3.11
Plot of X- and Y-axes rotational angles, shown here in degrees, which are used for transforming returned sonar mapping coordinates to give a flat seafloor. Year day 0.5 is 1200 EST, 01 January. Gaps in data are from either ground faults at the MVCO or bad sonar images due to high suspended sediment concentrations. The mine was deployed on year day 243 and repositioned on year day 338.

Once the rotational transformation angles giving the minimum standard deviation were found, they were used to transform the sonar coordinates into a corrected plot. The image shown above in figure 3.9 transforms to the following plot (fig 3.12).

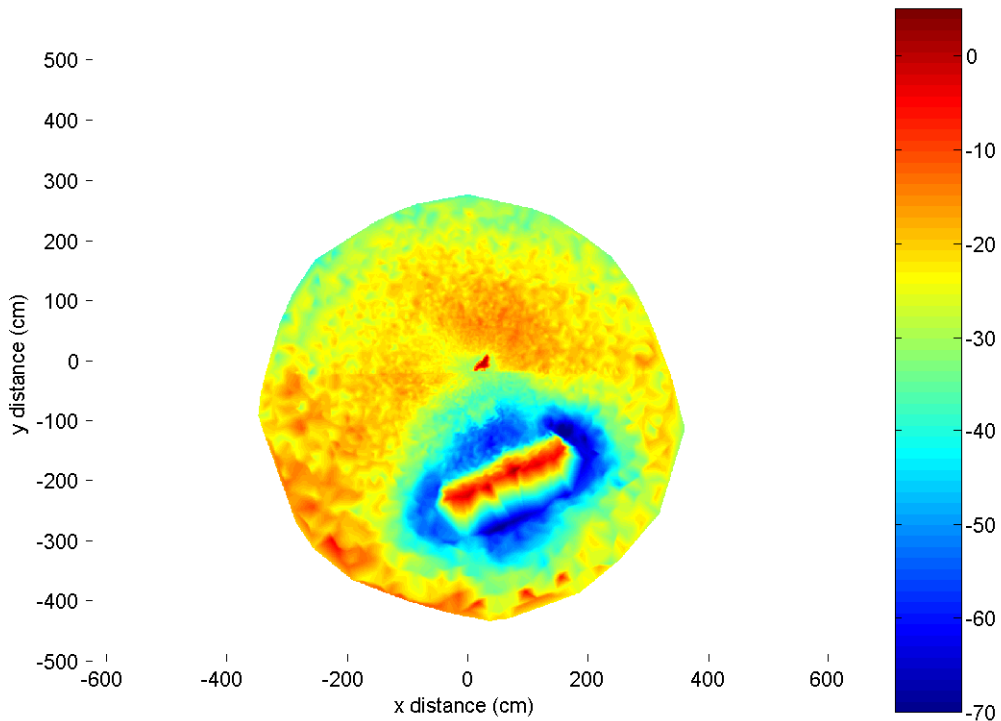


Figure 3.12
Plot of sonar image, transformed to produce a flat seafloor.
Color represents vertical height, in cm, above the seafloor
level at the base of the pole. Compare this plot with figure
3.2b, and the improvements are easy to see.

Comparing the original and corrected plots (figures 3.9 and 3.12, respectively), it is readily apparent that “1-2-3” transformation method corrects original plots, removing the effects of the leaning mounting system. To confirm this, a subtraction of the two plots should result in a plane sloping in a single direction, the actual angle of pole lean (fig 3.13).

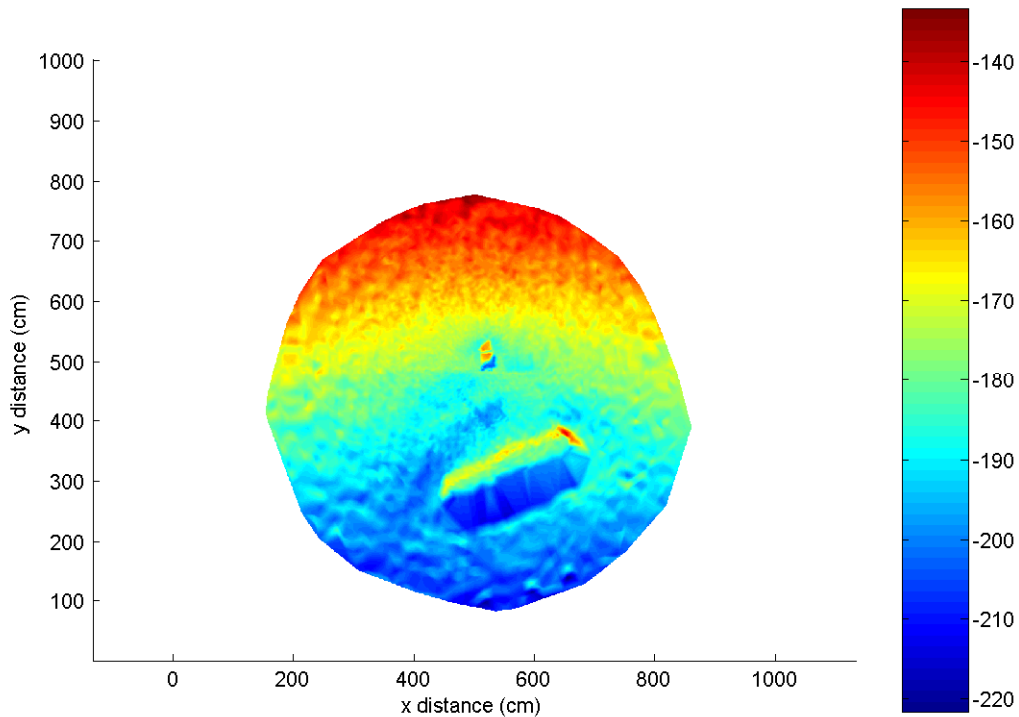


Figure 3.13
Plot of difference between the original and corrected sonar images. A sloping plane is clearly visible. Filtering artifacts, high frequency noise, and mine imaging techniques prevent the plane from being perfectly smooth, but this plot still proves the point that the “1-2-3” transformation method is effective.

Figure 3.13 also includes beam pointing corrections. The overall slope in the ambient seafloor is from transformational corrections. The “mine shadow” and high frequency noise are from beam pointing corrections.

4. SCOUR PIT DIMENSION RESULTS

The high resolution images provided by the 2 axis pencil beam sonar were mapped and interpolated onto an even two-dimension surface grid, using a Matlab 2-d interpolation routine. This allowed for quantitative measurements of the changing scour pit dimensions to be made. Dimensions sought were the scour pit mean and maximum depths, the surface area measured on a plane flush with the ambient seafloor, and total the scour volume. The scour pit was defined to be areas around the mine deeper than the ambient seafloor, which was measured in a part of the pencil beam hemisphere unaffected by the mine. Also sought was the height of the mine above the ambient seafloor plane, which when combined with the scour dimensions yields measurements of mine burial by depth.

4.1 Scour Pit Depth

Scour pit depth has been used in the past to analyze mine burial by depth, an important parameter when mine hunting with low grazing angle acoustic sensor systems (Trembanis et al. 2006). Both the mean and maximum depths were found as possible parameters to describe the size and extent of the scour pit for this reason (fig 4.1). Scour depth also proved to be a good indication of scour pit infilling.

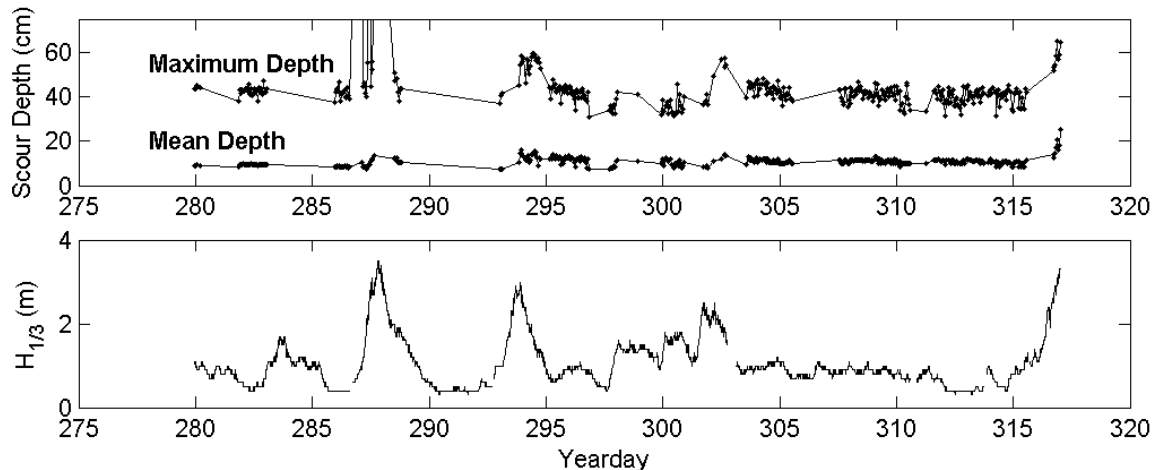


Figure 4.1

The top plot shows the mean and maximum depths of the scour pit below the ambient seafloor in cm. The range has been foreshortened to better show the variability in depth. Depths out of range between yeardays 285-290 are all around approximately 200 cm. The bottom plot shows the significant wave height, $H_{1/3}$, in m, measured at the MVCO. Yearday 0.5 is 1200 EST, 01 January.

Mean scour depth is the mean depth of all seafloor points within the scour pit, as defined above. Maximum scour depth is the single (1 cm^2) deepest point. The time period shown above does not include the entire mine deployment. As

mentioned before in section 2.2.2, initial sonar settings prevented the mine from being imaged at the very beginning of the deployment, and thus the above plot does not show the initial scour pit formation.

The scour pit has an initial mean depth of 8.9 cm and maximum depth of 43.4 cm below the undisturbed seafloor at the beginning of the usable sonar image period. Most of the significant changes to the mean scour depth after this occurred during and directly after storm events with significant wave heights greater than 2 m. The first large storm event peaked just before midnight on yearday 288 with a maximum significant wave height of approximately 3.4 m. While the storm approached and wave heights increased, the mean scour depth increased to 13.6 cm, and the maximum scour depth also increased to approximately 50.8 cm. There are several maximum scour depths in the 200 cm range; these numbers are most likely the results of high frequency noise left after filtering of the data set.

The second large storm event peaked just before midnight on yearday 294 with a maximum significant wave height of approximately 3 m. Usable data does not exist in this data set from late in yearday 288 until yearday 293. However, scour depths bracketing this time period suggest that there was a slight infilling event, decreasing the mean and maximum scour depths to about 7.5 cm and 36.9 cm, respectively. During the second storm event scour depths increased after the height of the storm when wave heights were decreasing. Mean scour depth increased to 16 cm and maximum scour depth increased to 59.4 cm.

There is approximately 6 days until the next storm event with significant wave heights greater than 2 m. Infilling events occurred again during this period, decreasing the mean and maximum scour depths to about 7.5-11.5 cm and 33.8-41.9 cm, respectively. The third and final storm event during the time period before the leaning sonar mounting pole effects became too large to overcome using transformational correction techniques peaked between noon of yearday 301 and noon of yearday 302, with a maximum significant wave height of approximately 2.5 m. Mean and maximum scour depths increased to about 14.2 cm and 57.2 cm, respectively. Infilling occurred again after the third storm event, reducing the mean and maximum scour depths to about 8.4-13.1 cm and 38.2-46.6 cm, respectively. This information is more clearly presented below in tabular form (table 4.1)

Yearday	280	288 (Storm I)	290-293	294 (Storm II)	295-301	301-302 (Storm III)	303-317
Mean Depth (cm)	8.9	13.6	7.5	16	7.5-11.5	14.2	8.4-13.1
Max Depth (cm)	43.4	50.8	36.9	59.4	33.8-41.9	57.2	38.2-46.6

Table 4.1
Progression of scour pit mean and maximum depths, in cm.
Specific time periods have been highlighted to show the
changes during storms and in the calm periods afterwards.
Yearday 0.5 is 1200 EST, 01 January.

The overall processes described in detail above is for scouring to occur right around the peak of storm events with significant wave heights greater than 2 m. Scour pit infilling took place between storm events, bringing the scour pit

almost back to its pre-storm depths. Scour pit surface area and total volume measurements will confirm these processes.

4.2 Scour Pit Area and Volume

4.2.1 Scour Pit Surface Area and Volume

To confirm scour and infilling changes as detailed by mean and maximum scour pit depth results, a look into the scour pit surface area, measured relative to a plane level with the ambient seafloor, as well as the total volume scoured below this level will be described (fig 4.2).

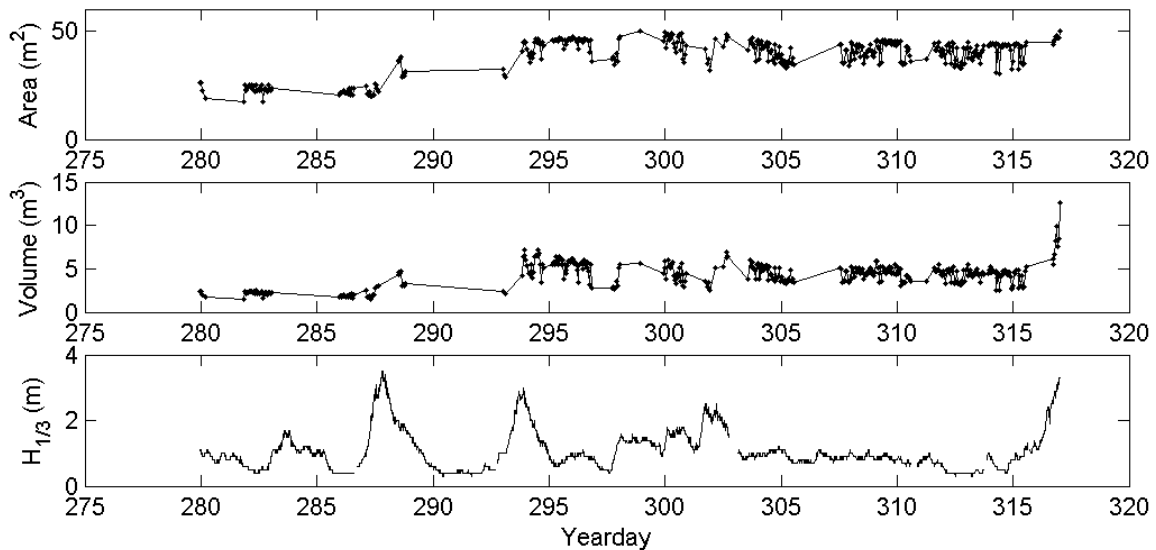


Figure 4.2

The top plot shows the area of the ambient seafloor scoured by the mine, in m². The middle plot shows the total volume scoured, in m³. The bottom plot shows the significant wave height, H_{1/3} in m, measured at the MVCO. Yearday 0.5 is 1200 EST, 01 January.

Again, initial sonar settings prevented the mine from being imaged at the beginning of the deployment. Consequently, the initial scour pit formation dimensions have not been measured. Compass data suggests that the mine rotated slightly to align perpendicular with the wave field, and accelerometer data

implies that the mine rolled into the scour pit created by the first storm early in the deployment. Also, the pressure difference between the MVCO and mine pressures sensors indicated that the mine sank approximately 50 cm during the first storm during the deployment (not imaged), then remained roughly level for the remaining time.

Scour surface area was found by measuring the number of cm^2 points in the interpolated two-dimension surface below the ambient seafloor. Scour volume is defined as the surface area multiplied by the individual depths below the ambient seafloor. The first usable sonar image gives a scour surface area of 26.2 m^2 and scour volume of 2.3 m^3 . The first large storm during imaged periods peaked just before midnight on yearday 288 with a maximum significant wave height of 3.4 m. While the storm approached and wave heights increased, the surface area increased to a peak value of 38 m^2 , and the volume increased to 4.7 m^3 . The second large storm event peaked just before midnight on yearday 294 with a peak significant wave height of approximately 3 m. Usable data does not exist from late in yearday 288 to yearday 293. However, the scour surface area and volume bracketing this time period suggest that there was a slight infilling event, decreasing the scour pit surface area to 29.7 m^2 and the volume to 2.3 m^3 just prior to the onset of the storm. After the second storm, the surface area showed slight fluctuations around 46 m^2 and the volume fluctuated around 6 m^3 . The scour surface area stayed around this level through the third storm on yearday 301 with a significant wave height of approximately 2.5 m, while the

volume decreased to about 5 m³ in the calm period following the third storm, suggesting a slight infilling event.

4.2.2 Scour Pit Area versus Depth

Scour area measurements were sought at differing depths in the scour pit to gain a better understanding of the scour processes taking place during storm events. Area measurements were found in the same manner as the total surface area, however reference levels have been changed to reflect the specific depths at which measurements were sought (fig 4.3). Scour pit areas have been measured in 5 cm reference level increments from the surface to 50 cm depth. As can be seen in figure 4.3, scour area values at depth fall off from the surface and follow the same overall trend as the surface, with little scour area below a depth of 35 cm.

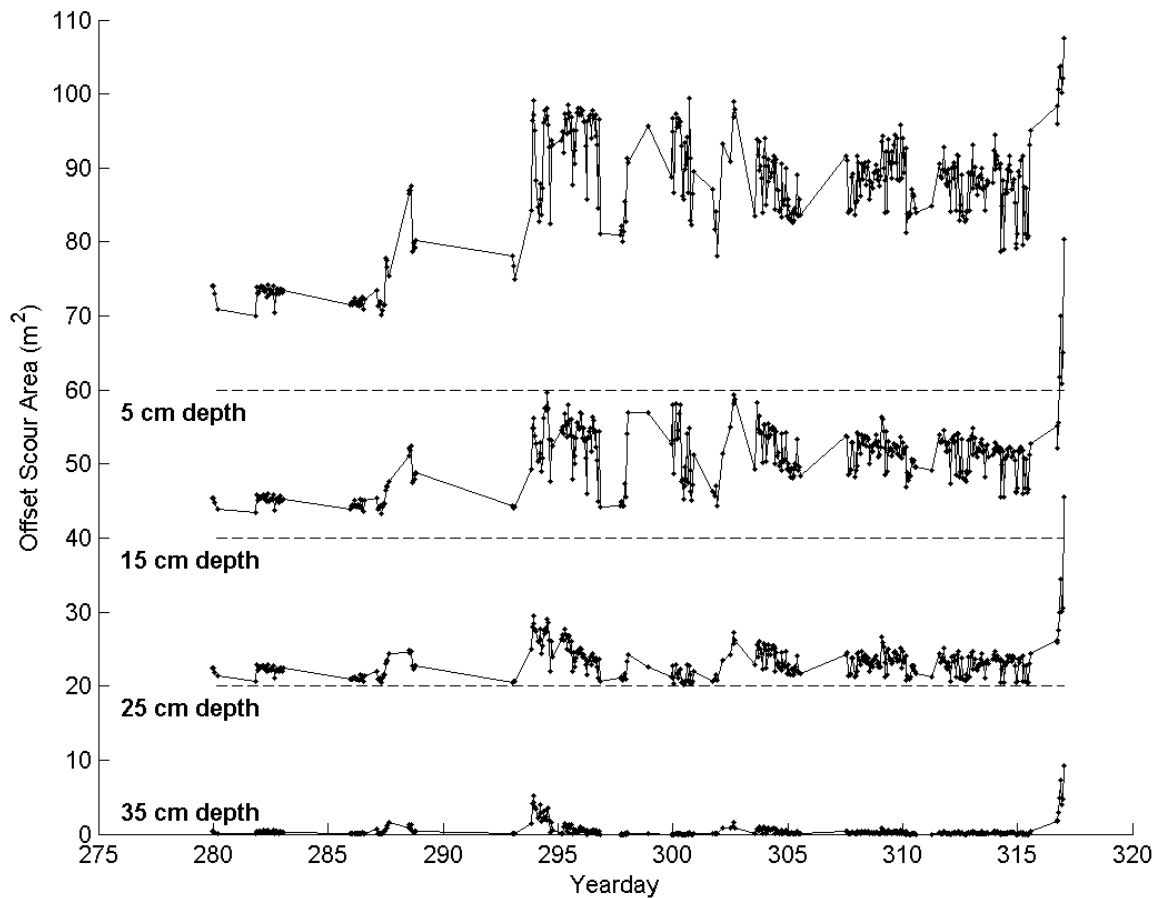


Figure 4.3
 “Offset” plot of scour pit areas, in m^2 , at differing depths. Levels of no scour offset are shown by dashed lines for each respective depth level. Note that the offset must be subtracted to obtain actual values. Yearday 0.5 is 1200 EST, 01 January.

A close examination of the scour pit area at 35 cm below the seafloor will reveal the behavior of the scour pit in relation to storm events much better than the total scour surface area, referenced to the ambient seafloor (fig 4.4).

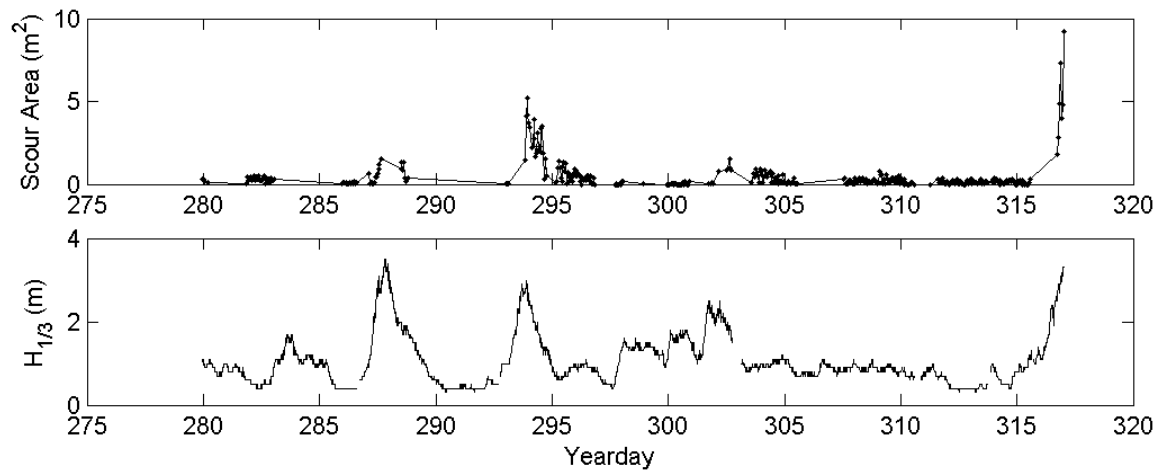


Figure 4.4
The top plot shows scour pit area at a depth of 35 cm below the ambient seafloor, in m². The bottom plot shows significant wave height, $H_{1/3}$ in m, measured at the MVCO for comparison. Yearday 0.5 is 1200 EST, 01 January.

Again, failure to image the initial mine burial and formation of the scour pit prevents a full analysis of scour properties, but other data suggests that a scour pit did form and the mine did roll into it, slightly below the far field seabed. Existing data does not provide precise measurements of the scour pit depth, so it is not possible to say whether the pit had scoured below 35 cm prior to mine imaging and subsequently infilled, or if it had never reached that level. All that can be concluded is that there is an initial scour area of 0.34 m² at a depth of 35 cm below the ambient seafloor at the start of sonar images.

Once the sonar was able to image the mine and its accompanying scour pit, some interesting characteristics are available. The scour pit area below 35 cm depth fluctuated around its initial value reaching a maximum area of 0.55 m² before the first imaged storm on yearday 288. During the storm, the area below

a depth of 35 cm scoured to approximately 1.5 m². There are no sonar measurements available until the onset of the second imaged storm on yearday 294. However, measurements bracketing this period suggest that there was an infilling event, bringing in sediment to fill in all holes at depths greater than 35 cm below the far field seabed. The scour area at this level is almost 0 m² before the second storm. During the second storm the area below 35 cm depth scoured to almost 5.2 m². Following the second storm, the scour area slowly decreased over a period of 3 days, infilling until there was no area scoured below a depth of 35 cm, and remained so until the third storm on yearday 301. The third storm scoured an area of 1.55 m² at 35 cm depth below the ambient seafloor. After the third storm, the scour pit again infilled, reducing the area below 35 cm to 0 m². This information is more clearly seen below in tabular form (table 4.2).

Yearday	280	288 (Storm I)	290-293	294 (Storm II)	295-301	301-302 (Storm III)	303-317
Surface Area (m ²)	26.2	38	29.7	46	46	46	46
Area below 35 cm (m ²)	0.55	1.5	0	5.2	0	1.55	0
Volume (m ³)	2.3	4.7	2.3	6	6	6	5

Table 4.2
Progression of scour pit total surface area in m², area at 35 cm below the ambient seafloor in m², and total volume in m³. Specific time periods have been highlighted to show the changes during storms and in the calm periods afterwards. Yearday 0.5 is 1200 EST, 01 January.

Comparing results from scour pit depth investigations with scour pit surface area and volume investigations allows one to conclude that the overall

process taking place is for high energy events associated with large storms to induce scouring around the mine, creating and enlarging the scour pit. In the calm periods following storms, the scour pit subsequently infills with sediment, partially burying the mine, as well as decreasing the overall depth and volume, while the surface area stays relatively the same.

4.3 Burial by Depth

4.3.1 Burial by Maximum Scour Pit Depth

A key characteristic of mine burial of particular importance to Naval operations is the depth at which the mine settles into its accompanying scour pit relative to the ambient far field seabed. If the scour pit is deeper than the diameter of the mine, then no portion of the mine will be visible above the ambient seafloor, making it difficult to acoustically detect at low grazing angles. This variable has been suggested in several works (7, 8) as percent burial by depth, and is expressed as:

$$BBD = 100 * \left(\frac{S_{\max}}{D} \right) \quad (6)$$

where BBD is percent burial by depth, S_{\max} is the maximum depth of the scour pit, and D is the diameter of the mine. Shown below is a plot of percent burial by depth, as calculated in equation (6) (fig 4.5).

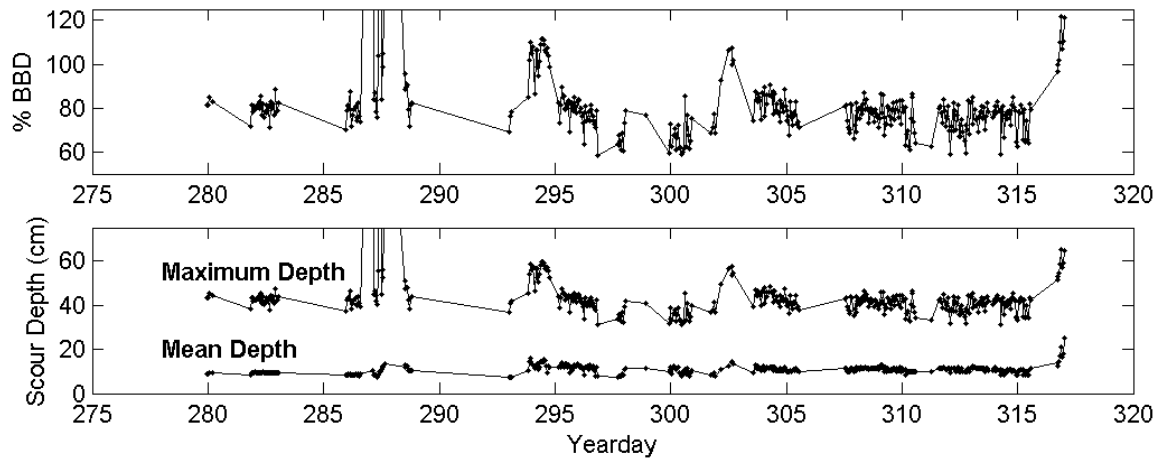


Figure 4.5
The top plot shows Percent Burial by Depth (equation 6). The bottom plot shows mean and maximum scour pit depths, for comparison. The range has been foreshortened to better show variability. High peaks due to noise have been cropped out, and are around 325% to 400%. Yearday 0.5 is 1200 EST, 01 January.

As equation (6) indicates, percent burial by depth is directly proportional to the maximum scour pit depth by a factor of $1 - \frac{\text{scour pit depth}}{\text{mine diameter}}$, which in this case is 53.3 cm. Thus, the trend of burial by depth is not surprising given the previously discussed scour pit dimension results. However, the actual values are. The mine is at 81.5% burial by depth at the start of available of sonar measurements. It increases to values between 110-120% around yeardays 293-295. It then drops down to values between 80-90%, then increasing again to a peak of 107.7% on yearday 302. It then decreases to values ranging between 60-90% for the duration of the measured deployment.

These results imply that the mine initially rolls deeper into the scour pit, sinking completely below the ambient seafloor, after storm events increase the

depth of the pit. However, percent burial by maximum scour depth fluctuates, implying a physically improbable trend in mine height exposure. Even though there has been evidence of cylindrical mines moving several diameters in the direction of wave propagation in other investigations (Inman and Jenkins 2002), there was no indication of significant mine movement in this deployment. Neither solid-state compass roll data nor changes in mine spatial location as seen from sonar images suggest that mine movement was large enough to roll up the side of the scour pit to a shallower depth to provide the percent burial by depths results shown in figure 4.5. Instead, it is most likely the ambient seafloor that is changing height as a result of migrating bedforms that is causing this apparent change in mine burial by depth. Thus, equation (6) is inadequate to capture the details of mine burial by depth since it does not account for changes in bed elevation.

4.3.2 Burial by Mean Scour Pit Depth

It can be possible for mines to shield the seafloor immediately below from the full forces of scouring effects creating a “pedestal” of sand on which the mine sits, elevated above the bottom of the scour pit. Thus, perhaps the maximum scour depth should not be used to find percent burial by depth, but rather the mean scour depth instead. This will change equation (6) to:

$$BBD_{mean} = 100 * \left(\frac{S_{mean}}{D} \right) \quad (7)$$

where S_{mean} is the mean scour pit depth. A plot of percent burial by depth, as calculated by equation (7) is shown below (fig 4.6).

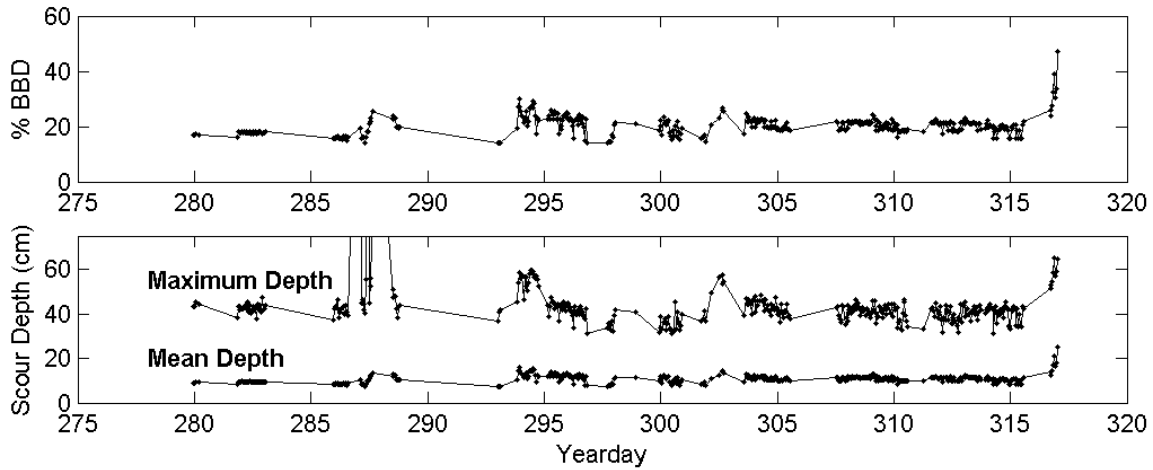


Figure 4.6
The top plot shows Percent Burial by Depth (equation 7).
The bottom plot shows mean and maximum scour pit depths, for comparison. Yearday 0.5 is 1200 EST, 01 January.

The mine is at 16.7% burial by depth at the start of available of sonar measurements. It increases to values between 20-30% around yeardays 293-295. It then drops down to values between 17-22%, then increasing again to a peak of 26.6% on yearday 302. It then decreases again to values ranging between 19-24% for the duration of the measured deployment.

This time, using equation (7) to calculate percent burial by depth gives a physically more realistic trend. The mine scours and, then percent burial by

mean scour depth shows that mine height exposure increased during calm periods. During the height of storm events the mine scours deeper followed by percent burial by mean scour depth decreasing again. In general, the mine settles from an initial value of 16.7% burial by depth to a final value of 22% burial by depth, showing an overall trend of the mine slowly sinking deeper into the scour pit.

4.3.3 Burial by Mine Height

Again, there are problems with calculating percent burial by depth through mean scour pit depth measurements. The highest percent burial by depth is 30%, meaning that approximately 37.3 cm of the 53.3 cm diameter mine is exposed above the ambient seafloor. Sonar imaging does not support this claim, as the mine is never seen to sit that far above the ambient seafloor in any image. Even including the extensive image corrections required in this deployment, a 37.3 cm elevation would be clearly evident, if that were the case as supported by values in figure 4.6. Thus, a third method of calculating percent burial by depth is now proposed, based not on scour pit depth, but rather on the mine height above the far field seabed:

$$BBD_{mh} = 100 * \left(\frac{D - mh}{D} \right) \quad (8)$$

where mh is the height of the mine above the ambient seafloor. This method is possible when using high resolution sonar systems. A plot of percent burial by depth, as calculated by equation (8) is shown below (figure 4.7).

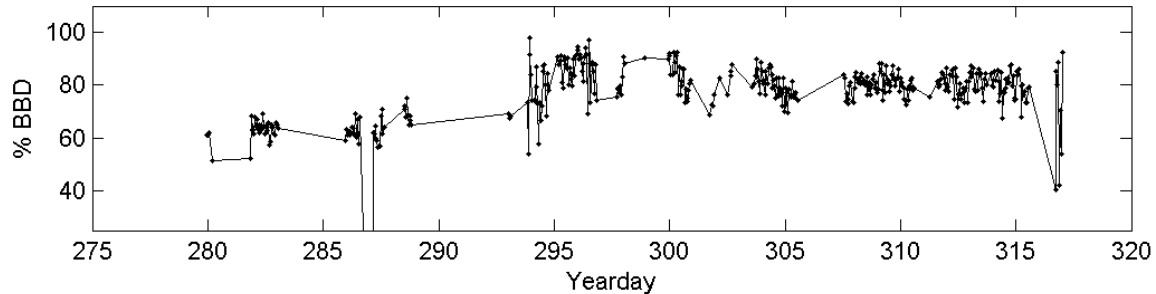


Figure 4.7
Plot of Percent Burial by Depth (equation 8). The range has been foreshortened to better show variability. Yearday 0.5 is 1200 EST, 01 January.

Initial values of percent burial by depth, as calculated using equation (8), at the beginning of available sonar measurements vary between 56.6%-60.1%. It increases to values between 68-93% between yeardays 293-295. It drops down to 80.1% during the infilling event after the second storm, rises to 90.4% during the induced scour from the third storm, and drops down to steady state values between 75-85% during the calm period following the third storm.

While these values do exhibit the same fluctuating trends as other methods of calculating percent burial by depth, the deviations are not as great. This gives a physically more realistic picture of what the mine can be expected to do. Also, the maximum burial by depth percentage of 92.7% equates to

approximately 3.9 cm mine exposure above the far field seabed. This value is verified by pencil beam sonar measurements.

To further explain the fluctuations in figure 4.8, it is necessary to describe the algorithm used find the mine height. After the sonar data was interpolated and mapped onto a 2-d grid, an area was defined that generally encompassed the mine and scour pit for the majority of the deployment. The mine height was defined to be the maximum height within this area above the ambient seafloor. Thus, any high frequency noise missed by previous filtering will be represented in this measurement. However, even with this potential for error, the overall trend of percent burial by depth calculated using the height of mine above the ambient seafloor gives a much better look into the mine's movements and actions, where storm induced scour causes the mine to sink below the seafloor into the scour pit to a point where turbulence effects from the reduced exposed mine height mimic those of the surrounding seafloor bathymetry, allowing the mine to reach a constant level with little change. Operationally, Naval mine hunting platforms will be searching for objects projecting above the local seafloor. Thus, modeling burial by depth as a function of mine height will better translate directly into fleet uses.

5. DISCUSSION and CONCLUSION

5.1 Hydrodynamic Mine Forcing and Bed-Load Flux

5.1.1 Inertial and Drag Hydrodynamic Forces on the Mine

Changing scour pit dimensions have already been related to the wave climate, specifically large storms, with significant wave heights greater than 2 m. These storms act to enlarge the scour pit in both depth and area and ultimately allow the mine to settle deeper into the pit, while calm periods following storms permit sediment to infill into the pit, burying the mine. Scour pit development is essential to the overall scour-infill-bury process, however, the mine must roll into the scour pit formed around it. Mines have been seen to sit on “pedestals” of sand, elevated slightly above the deepest depths of the scour pit. A brief look at the hydrodynamic forcing on the mine will answer the question of what causes the mine to roll off its pedestal deeper into the scour pit. Specifically, large bottom velocities associated with storm events where significant wave heights exceed the 2 m threshold are compared with the calm periods between storms where waves are much smaller and have higher frequencies, where water particle acceleration effects are dominant. The hydrodynamic forcing on the mine in unsteady flow is found using the Morrison equation (Sorensen, 1978). The Morrison equation is defined as:

$$\begin{aligned}
F &= \frac{C_D}{2} \rho_w A U^2 + C_M V \rho_w \frac{dU}{dt} \\
U &= \max | \vec{U}_{current} \pm \sqrt{2} \vec{U}_{rms} | \\
\frac{dU}{dt} &= \frac{2\pi\sqrt{2}U_{rms}}{T}
\end{aligned} \tag{9}$$

where F is the total hydrodynamic force in unsteady flow, C_D and C_M are the coefficients of drag and mass for circular cylinders, respectively, ρ_w is the fluid density, A and V are the mine's cross sectional area and volume, respectively, exposed normal to the fluid flow, U is the near bottom fluid velocity from combined waves and mean current, and $\frac{dU}{dt}$ is the fluid acceleration from waves only.

The near bottom fluid velocity was measured by the RDI ADCP at the MVCO. The mean current velocity, $U_{current}$, is the velocity measured in the deepest range bin of the ADCP, and the wave velocity, $\sqrt{2}U_{rms}$, is found from the root mean squared velocity from the deepest range bin. The total bottom velocity was found from the maximum magnitude of the vector addition of both components, allowing for both positive and negative wave velocities, to account for the orbital velocity of waves. Only wave velocities were used to find $\frac{dU}{dt}$, as the current velocities are mainly tidal driven and don't vary much over the time scale. The first term in equation (9) deals with drag effects, while the second term deals with inertial effects.

A plot of the drag and inertial hydrodynamic forces on the mine is shown below (figure 5.1). Many of the oceanographic and mine dimension values are detailed in chapter 2. C_D and C_M were chosen from typical values of circular cylinders under similar Reynolds number conditions as the mine, and are equal to 1 and 2, respectively. The drag force is negligible except during the three storm events. The drag force fluctuates around 0 with large excursions of about 10 N during calm periods, and the maximum drag force peaks at approximately 120 N during the first storm, and at about 50 N and 45 N during the second and third storms, respectively. While the inertial force is also relatively minimal during calm periods, fluctuations are much larger, with excursion magnitudes of about 50 N during calm periods. Peak inertial force values during storms are much larger than those of the drag force. The maximum inertial force peaks at approximately 170 N right before the significant wave heights from the first storm reach their maximum height in the immediate deployment area and at about 100 N the second and third storms.

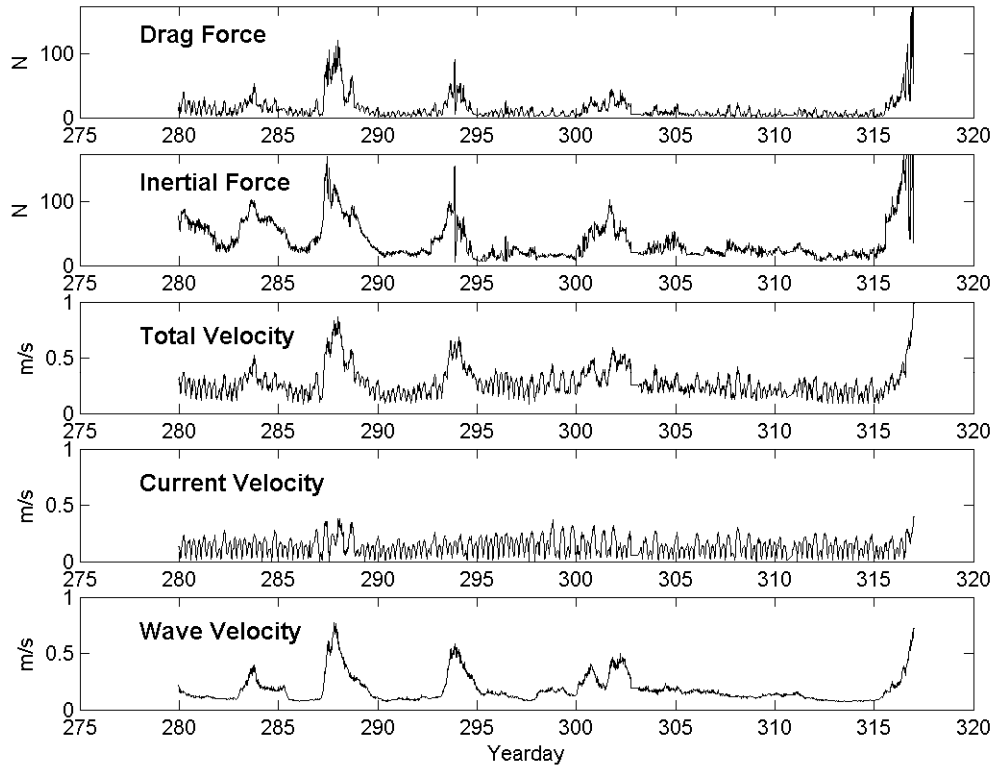


Figure 5.1

The top plot shows the drag force in N, from equation (9). The second plot shows the inertial force in N, from equation (9). The scale of both panels is the same. The last three plots contain the total bottom velocity, the bottom current velocity, and the bottom wave velocity, respectively. All velocity values are in m/s. Yearday 0.5 is 1200 EST, 01 January.

Each force calculation shows peak values during storm events with relatively no forcing during calm periods between storms. The inertial force typically peaks during the buildup of the storm before maximum significant wave heights reach the deployment area due to higher frequency waves at the beginning of the storm, whereas the drag force peaks during the height of the storm when the combined wave and current velocities are greatest. The

magnitudes of each force component are similar, yet the relative timing is different. This leads to the hypothesis that both inertial forces associated with large water particle accelerations and drag forces associated with large water velocities from high wave heights act together to force the mine off its pedestal into the deeper depths of the scour pit. The initial movement of the mine is due to water particle accelerations which act to “rock” the mine back and forth. Significant movement away from the pedestal is possible since the orbital velocities have diameter magnitudes of approximately 1 to 2 m. The drag force peaks later in each storm than the inertial force. Although it does fluctuate in magnitude, it remains positive for most of each storm. This equates to a “push” in a constant direction throughout the duration of each storm, causing the mine to roll the rest of the way off the pedestal, completing the movement initiated by the inertial rocking of the mine. Together, these two conclusions support this hypothesis.

5.1.2 Wave Averaged Net Bed-Load Flux

Once the mine has been forced off its pedestal into the deeper depths of the scour pit, infilling sediment can bury the mine in the final stage of the scour-infill-bury process. It has already been shown in chapter 4 that changes in mine burial and scour pit dimensions follow the wave height. One reason that the change in scour pit dimensions follow the wave height and not the combined wave and current velocities has been described in Grant and Madsen, 1979, and

is summarized here. The boundary shear stress from current and tidal motion is generally an order of magnitude smaller than the boundary shear stress from wave induced orbital velocities of similar magnitude. This can be easily visualized by considering the small wave boundary layer in comparison with the larger boundary layer from current flow. Thus, waves can stir up significant amounts of sediment from the seafloor, but do not provide much net transport of the sediment. Large currents, on the other hand, can transport suspended sediment a large distance, but often does not initiate motion of non-suspended sediment. Wave and current fluid motion combined create an effective sediment transport mechanism, where the waves entrain sediment into fluid, making it available for transport by even a weak current.

An expansion on this general explanation deals with the bed-load sediment transport flux. Calculations of the wave averaged bed-load flux will highlight time periods during the deployment cycle when both scour and infilling of the scour pit occurs. This calculation was made using the Bagnold, Bowen, and Bailard “BBB energetics” model (Zhao and Kirby, 2005; Hass and Hanes, 2004). The BBB energetics model is defined as:

$$\begin{aligned}
\langle \vec{q} \rangle &= \frac{\langle \vec{i} \rangle}{g(\rho_s - \rho_w)} \rho_s \\
\vec{i} &= \rho_w c_f \frac{\varepsilon_b}{\tan \phi} \left[|\vec{U}|^2 \vec{U} - \frac{\tan \beta}{\tan \phi} |\vec{U}|^3 \right] + \rho_w c_f \frac{\varepsilon_s (1 - \varepsilon_b)}{w} \left[|\vec{U}|^3 \vec{U} - \frac{\varepsilon_s (1 - \varepsilon_b)}{w} \tan \beta |\vec{U}|^5 \right] \\
c_f &= \exp \left[5.213 \left(\frac{r}{a_o} \right)^{0.191} - 5.977 \right] \\
r &= 2.5D50 \\
a_o &= \frac{U_{wave}}{\omega}
\end{aligned} \tag{10}$$

where $\langle \vec{q} \rangle$ is the wave averaged net bed-load flux, \vec{i} is the sediment transport rate, c_f is the bottom friction coefficient, r is the bottom roughness, and a_o is the amplitude of the bottom wave orbital velocity excursions. The first sediment transport term represents bed-load sediment transport, and the second term represents suspended sediment transport. ρ_s is the sediment density, ρ_w is the fluid density, g is gravitational acceleration, ε_b and ε_s are the bed-load and suspended load efficiencies, respectively, ϕ is the sediment particle friction angle, β is the bottom slope angle, U is the near bottom fluid velocity from combined waves and mean current, w is the sediment fall velocity, $D50$ is the sediment mean grain size, U_{wave} is the near bottom fluid velocity from waves only, and ω is wave frequency.

Plots of bed-load flux components are shown below (figure 5.2). The sediment density (ρ_s) is 2661 kg/m³, the mean grain size ($D50$) is 180 μ m, ε_b and ε_s are 0.1 and 0.01, respectively, the fall velocity (w) is 0.0203 m/s, the seafloor is

assumed to be flat ($\beta=0$), and the particle friction angle (ϕ) is approximately 32° . Other oceanographic values are detailed in chapter 2. The maximum bed-load transport flux is approximately 0.08 kg/m/s, the maximum suspended sediment transport flux is approximately 0.16 kg/m/s, and the maximum total flux is approximately 0.24 kg/m/s. These peak values occur during the height of the first storm, with smaller local peaks during the second and third storms. Calm periods between storm events typically have almost no bed-load flux.

One possible mechanism for scour pit infilling and mine burial is that the suspended sediment transport flux drives scour out of the scour pit, while bed-load transport flux drives the infilling of the scour pit. When water velocities are energetic enough to create a turbulent the boundary layer around the mine, sediment is entrained well into the water column, initiating suspended sediment flux. This allows the sediment to rise out of the scour pit above the ambient seafloor, and be washed away. Thus there is a net movement of sediment out of the scour pit, resulting in an enlarged scour pit in depth, area, and volume. Thus, highly turbulent flow over a short period of time is able to scour large amounts of sediment in the immediate local vicinity of the mine. The highly angular geometry around the mine will only further intensify the turbulent effects.

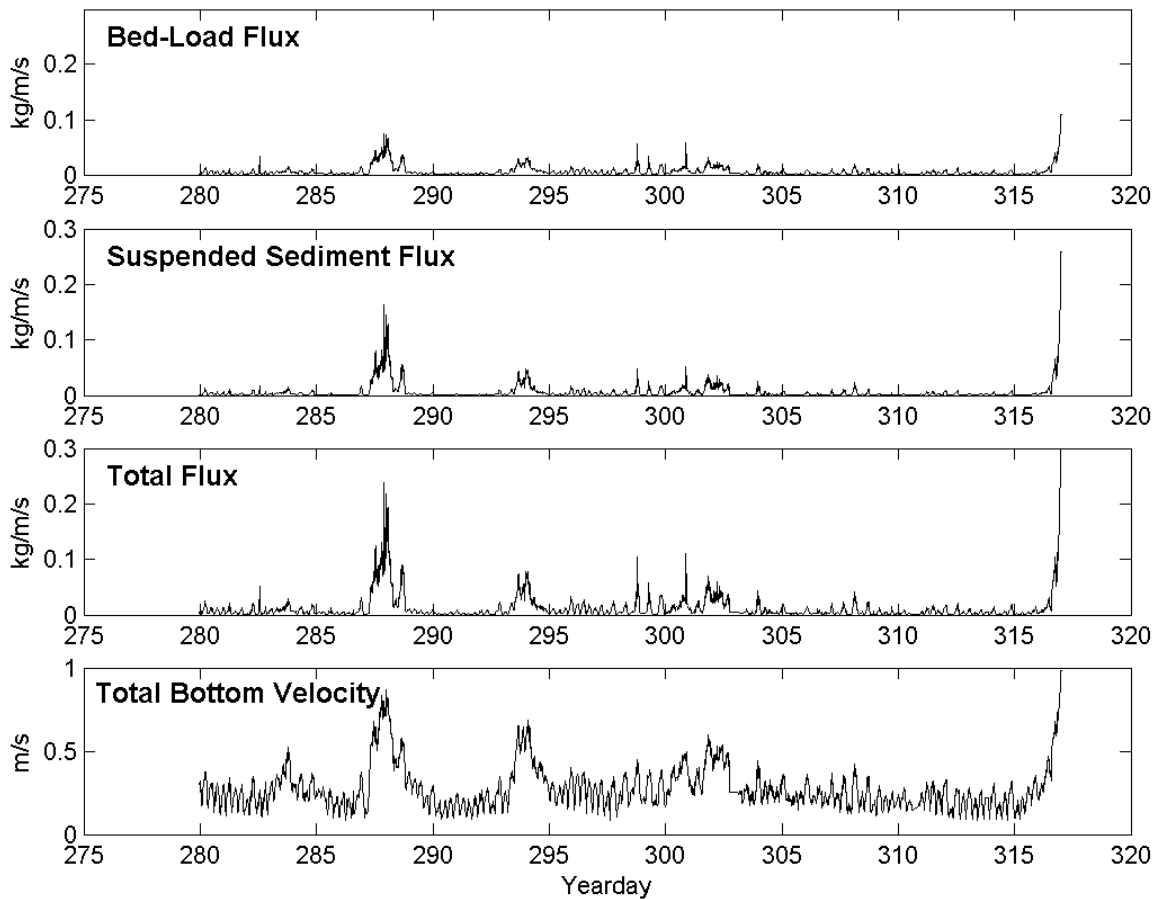


Figure 5.2

The top plot shows the bed-load flux from bed-load sediment transport in kg/m/s. The second plot shows the bed-load flux from suspended sediment transport in kg/m/s. The third plot shows the total bed-load flux, a combination of both bed-load and suspended sediment transport, in kg/m/s. The bottom plot shows the total bottom velocity, from combined wave and current velocities, in m/s. Yearday 0.5 is 1200 EST, 01 January.

During calm periods, when water velocities are not large enough to suspend sediment into the water column, bed-load transport flux dominates. This is a fluctuating transport of sediment close to the seafloor, driven mainly by the waves. When this sediment encounters the scour pit, some sediment falls below the ambient seafloor (roughly the level at which it was traveling) into the

scour pit. Relatively steady tidal current flow is dominant between storms. The tidal flows around the mine at this time will have a large boundary layer on the mine and seabed. Thus stresses are weak and there is little chance for sediment to be entrained and suspended into the flow. Sediment inside the scour pit is relatively protected from water movement. What little sediment motion is initiated does not rise high enough in the water column to escape the scour pit. Thus, can infilling occur, burying the mine.

An estimation of the total bottom water velocity at which the sediment transport flux domain changes from bed-load driven to suspended sediment driven is useful in determining periods of both scour pit infilling and scour to compare with the 2 axis pencil beam sonar images (figure 5.3). The values for bed-load and suspended sediment transport flux (equation 10) are plotted as a function of total bottom velocity (U) only. The wave period (T) was held constant at 6 sec. This values for the wave period was chosen to be close to the mean wave period throughout the deployment. Results for other wave periods are not shown because they give highly similar values. The mean grain size (D_{50}) is $180\text{ }\mu\text{m}$, a good approximation of the grain size in the immediate mine deployment area.

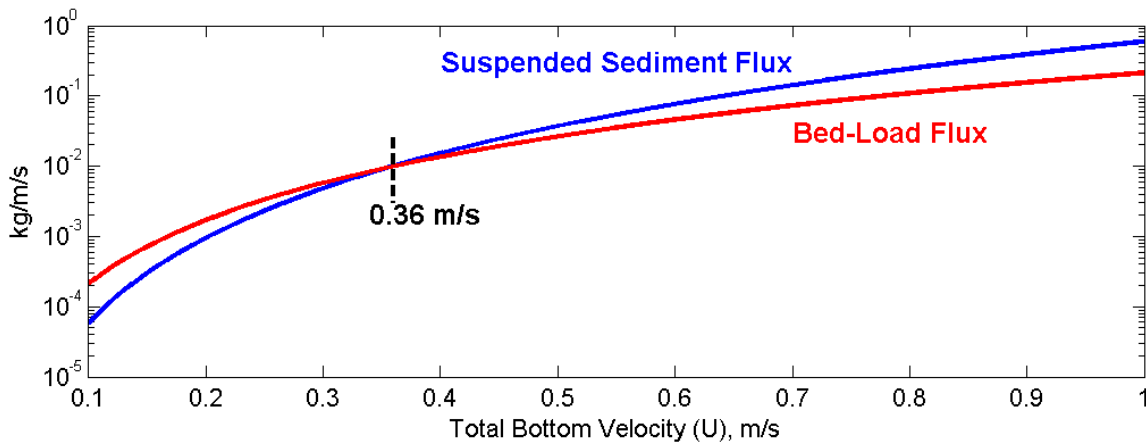


Figure 5.3
Semi-logarithmic plot of suspended sediment transport flux and bed-load transport flux in kg/m/s versus total bottom velocity in m/s, calculated using equation (10), where $T = 6$ sec, and $D50 = 180 \mu\text{m}$. Bed-load transport flux is dominant for bottom velocities less than 0.36 m/s. For bottom velocities larger than 0.36 m/s, suspended sediment transport flux is dominant.

As seen above in figure 5.3, bed-load transport flux is dominant when total bottom velocities (combined wave and current velocities) are less than 0.36 m/s. This is when infilling should occur. When bottom velocities are greater than 0.36 m/s, suspended sediment transport flux dominates, and scour around the mine should occur. The ratio of bed-load transport flux to suspended sediment transport flux (BL/SS) is the ratio of the respective values of bed-load transport driven flux to suspended sediment transport driven flux. This ratio, calculated with actual measured values, will be used as an indication of whether the mine and scour pit are undergoing either scour or infilling. BL/SS values greater than 1 indicate an infilling period and values less than 1 indicate a scour period.

5.2 Scour Pit Progression during Storm Events

The scour-infill-bury process described above can be easily understood by examining returned sonar images. Sonar images have been selected to bracket storms, encompassing both the times of high scour, as well as the following infilling and burying periods (figures 5.4-5.6).

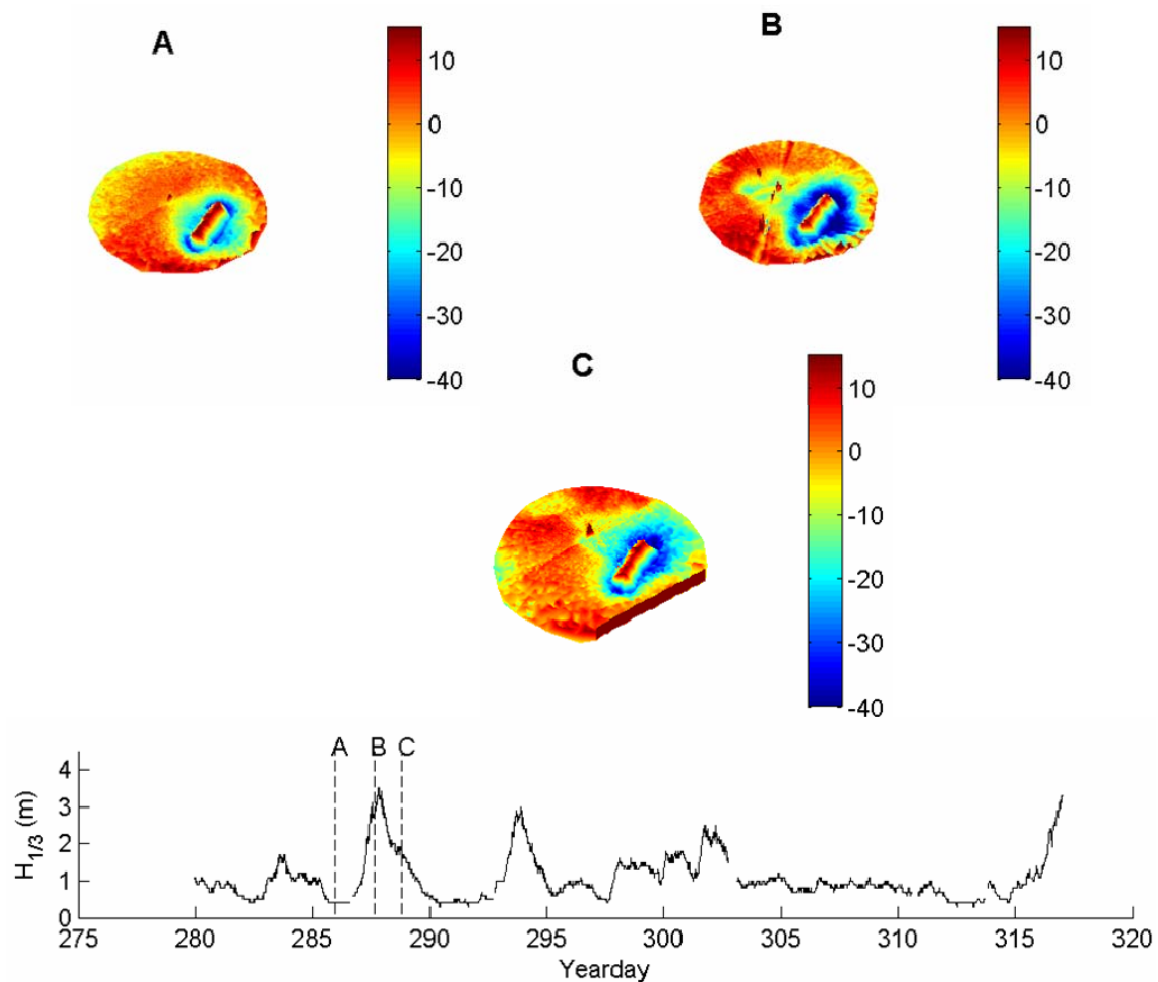


Figure 5.4
 Plots showing sonar images returned during the first storm event depicting the progression of scour pit formation and the subsequent infilling and mine burial (A) before the storm, (B) at the peak of the storm, and (C) immediately after the storm. Color depicts height above the ambient seafloor. Wave heights are shown for comparison. Yearday 0.5 is 1200 EST, 01 January.

The first major storm event (figure 5.4) during the imaged deployment period shows the mine sitting in a preexisting well defined scour pit prior to the storm. The top of the mine is exposed well above the ambient seafloor (panel A). The total bottom velocity is 0.18 m/s, which gives an actual bed-load to

suspended sediment transport flux ratio (BL/SS) of 4.1, meaning that scour pit infilling is taking place in the calm period prior to the storm's arrival. The scour pit is increased in depth as well as area, both at the surface and at a depth of 35 cm below the seafloor, as the storm arrives (panel B). The total bottom velocity is 0.51 m/s with a BL/SS ratio of 0.71. This means that there is significant scour occurring around the mine at the height of the storm, confirming sonar measurements. The mine also sinks relative to the far field seabed. Infilling resumes almost immediately after the storm subsides (panel C). Mean depth and the area of the scour pit at 35 cm depth provide good indications of this infilling. The total bottom velocity is 0.30 m/s, giving a BL/SS ratio of 1.35, again confirming sonar measurements. The mine also sinks deeper below the seafloor. Actual dimensions are presented below (table 5.1).

Panel and yearday	A (285.96)	B (287.63)	C (288.83)
Mean Depth (cm)	8.3	13.6	10.6
Max Depth (cm)	37.5	191.7 (error)	43.8
Surface Area (m ²)	20.7	21.1	31.4
Surface Area Below 35 cm (m ²)	0.0	1.5	0.3
Volume (m ³)	1.7	3.0	3.3
Mine Height (cm)	21.9	19.1	18.8
Water Velocity (m/s)	0.18	0.51	0.30
BL/SS	4.1	0.71	1.35

Table 5.1
Progression of scour pit dimensions during the first storm
with a significant wave height greater than 2 m. Yearday 0.5
is 1200 EST, 01 January.

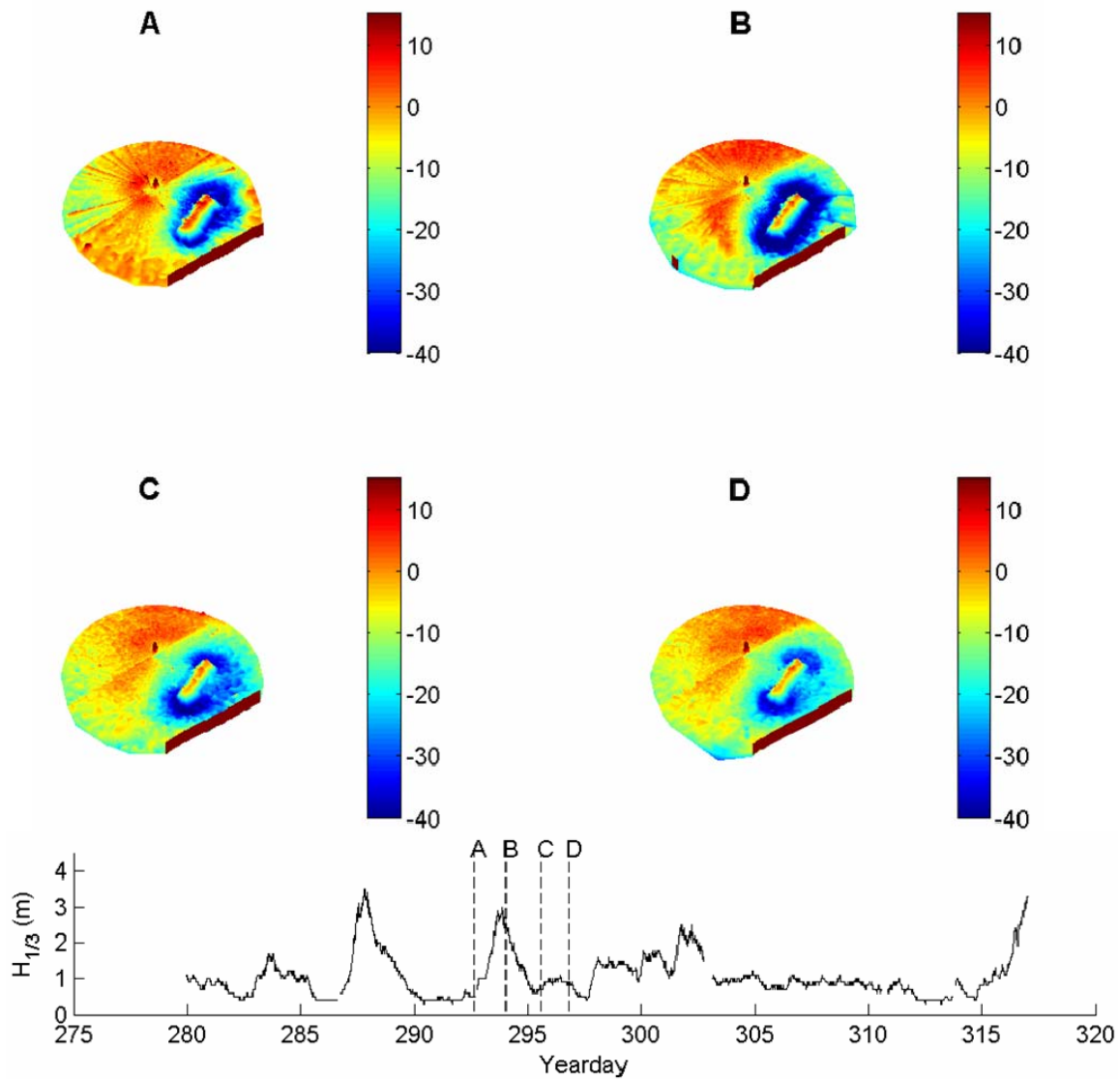


Figure 5.5
 Plots showing sonar images returned during the second storm event depicting the progression of scour pit formation and the subsequent infilling and mine burial (A) before the storm, (B) at the peak of the storm, (C) immediately after the storm, and (D) in the calm period 2 days after the storm. Color depicts height above the ambient seafloor. Wave heights are shown for comparison. Yearday 0.5 is 1200 EST, 01 January.

The second major storm event (figure 5.5) during the imaged deployment period shows that the scour pit has continued to infill from panel C of figure 5.6, centering the scour pit around the mine (panel A). The total bottom velocity at this time is 0.16 m/s, giving a BL/SS ratio of 3.27. The top of the mine is still exposed well above the ambient seafloor at this point. As the storm peaks, the scour pit is increased in surface area as well as depth (panel B), causing the mine to sit lower in the scour pit with less exposure above the ambient seafloor. The total bottom velocity is 0.64, giving a BL/SS ratio of 0.67, confirming the scour results from sonar measurements. Infilling starts almost immediately after the storm passes and wave energy subsides (panel C). The total bottom velocity is 0.22 m/s with a BL/SS ratio of 1.80. The overall depth decreases, yet surface area and volume continues to increase, an indication that some of the infilling sediment originated from erosion of the side walls of the scour pit. The mine also continues to sink lower into the scour pit. One and a half days after the storm (panel D), the scour pit has received a significant amount of sediment around the longitudinal axis of the mine, while the area around the ends of the mine receives little, remaining at its post-storm depths. The BL/SS ratio is 1.64, from a total bottom velocity of 0.23 m/s. This time there is only a slight increase in scour surface area, and a decrease in total volume, indicating that the majority of the infilling sediment originated from outside of the scour pit. Actual dimensions are presented below (table 5.2).

Panel and yearday	A (292.63)	B (294.04)	C (295.58)	D (296.79)
Mean Depth (cm)	7.5	12.8	13.1	12.1
Max Depth (cm)	41.7	57.5	44.5	42.1
Surface Area (m ²)	28.7	41.4	45.9	45.9
Surface Area Below 35 cm (m ²)	0.0	3.4	1.3	0.3
Volume (m ³)	2.2	5.5	6.0	5.5
Mine Height (cm)	16.9	13.7	5.0	6.5
Water Velocity (m/s)	0.16	0.64	0.22	0.23
BL/SS	3.27	0.67	1.80	1.64

Table 5.2
Progression of scour pit dimensions during the second storm with a significant wave height greater than 2 m. Yearday 0.5 is 1200 EST, 01 January.

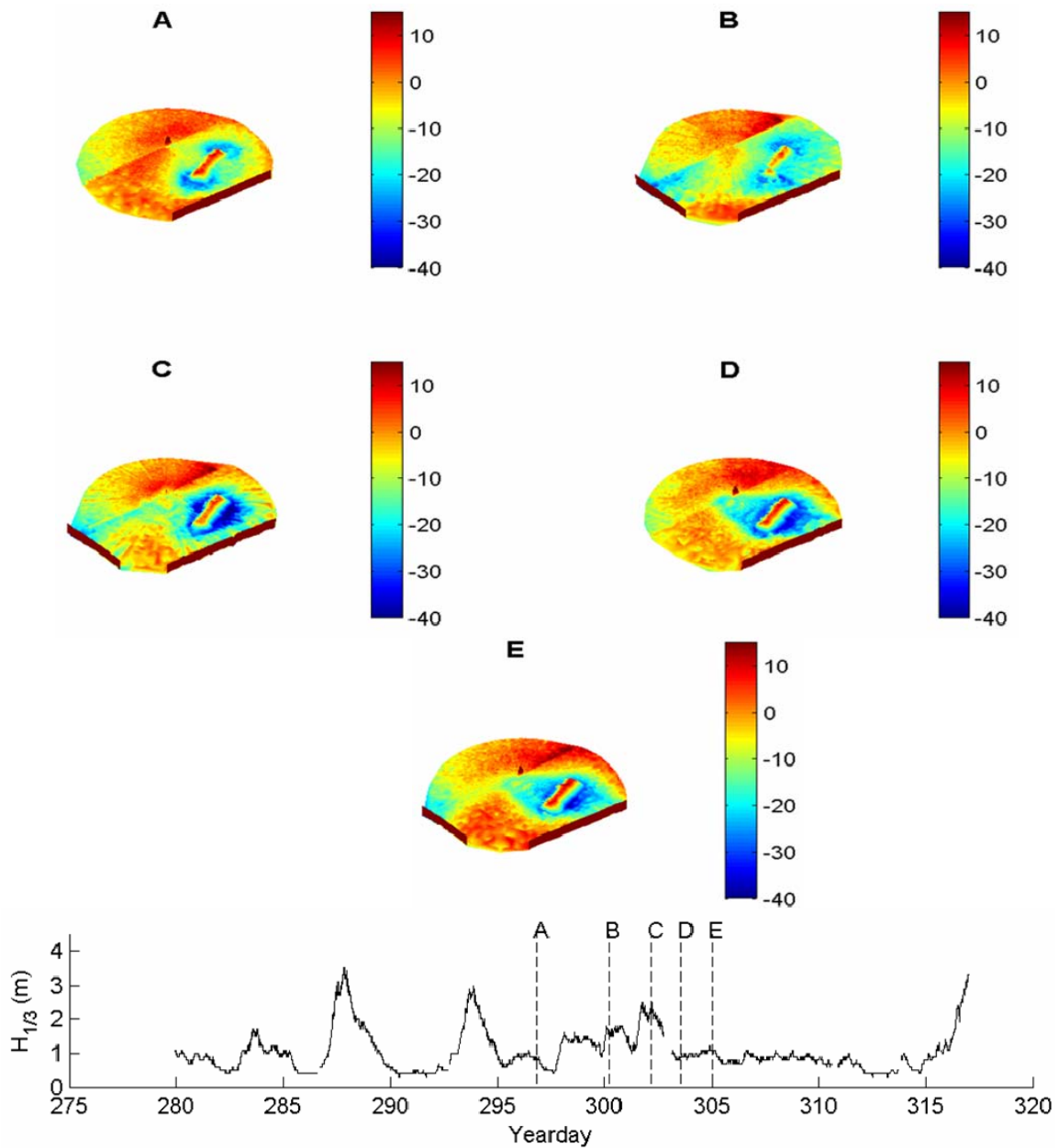


Figure 5.6
 Plots showing sonar images returned during the third storm event depicting the progression of scour pit formation and the subsequent infilling and mine burial (A) before the storm, (B) at the peak of the storm, (C) immediately after the storm, and (D) in the calm period 2 days after the storm. Color depicts height above the ambient seafloor. Wave heights are shown for comparison. Yearday 0.5 is 1200 EST, 01 January.

The third and final major storm event (figure 5.6) during the imaged deployment period shows the scour pit with significant sediment accumulation around the longitudinal axis of the mine, while little has collected near the ends (panel A). The total bottom velocity is 0.16 m/s with a BL/SS ratio of 2.43. This confirms the visually seen infilling in panel A of figure 5.8. The top of the mine appears closer to the sonar than its previous depth directly after the second storm. A reasonable explanation for this is that there was a major shift in the ambient seafloor, possibly from the passage of a large scale bedform outside of the range of the 2 axis pencil beam sonar.

The third storm did not strengthen as quickly as the first two; it took approximately 4 days to reach heights greater than 2 m after the storm first arrived. Infilling continued to take place during this time around the longitudinal axis of the mine (panel B), while the turbulence associated with the unsteady orbital wave velocities scoured around the ends of the mine, increasing depth, area, and volume. The total bottom velocity was 0.24 m/s with a BL/SS ratio of 1.81 during this period, meaning that overall infilling outweighed scour. This highlights the necessity for wave heights to be greater than 2 m to induce any significant scour around the mine, as the significant wave height is only 1.6 m at this time. Once the storm did break the 2 m threshold (panel C), the infilling sediment around the mine was scoured away, and the scour pit resembled its pre-infilling dimensions. The total bottom velocity is 0.47 m/s, giving a BL/SS ratio of 0.82. Infilling resumed immediately after the storm subsided (panel D).

Depth, area, and volume all decreased. The total bottom velocity is 0.21 with a BL/SS ratio of 2.28. Infilling can be seen to continue a few days after the storm has passed (panel E). The total bottom velocity is 0.33 m/s with a BL/SS ratio of 1.26, showing that infilling continued to take place. One notable characteristic during this storm is the fact that the mine height exposure above the ambient seafloor appears to increase after the storm has started. Again, this is most likely from the movement of a large scale bedform out of the immediate deployment area, decreasing the actual depth of the ambient seafloor below the sonar, and not from the mine rising up within the scour pit. Actual dimensions are presented below (table 5.3).

Panel and yearday	A (296.83)	B (300.21)	C (302.17)	D (303.58)	E(305.00)
Mean Depth (cm)	7.6	11.1	10.9	9.2	10.0
Max Depth (cm)	31.0	32.5	49.3	39.5	41.9
Surface Area (m ²)	36.0	46.1	46.5	41.1	37.1
Surface Area Below 35 cm (m ²)	0.0	0.0	0.8	0.1	0.1
Volume (m ³)	2.7	5.1	5.1	3.8	3.7
Mine Height (cm)	13.6	8.2	9.3	11.1	14.7
Water Velocity (m/s)	0.16	0.24	0.47	0.21	0.33
BL/SS	2.43	1.81	0.82	2.28	1.26

Table 5.3
Progression of scour pit dimensions during the third storm
with a significant wave height greater than 2 m. Yearday 0.5
is 1200 EST, 01 January.

5.3 Conclusions

An instrumented mine was placed in approximately 12 m water depth on fine quartz sand south of the island of Martha's Vineyard near the Martha's Vineyard Coastal Observatory. 2 axis pencil beam sonar measurements are available during 3 large storms during the deployment of the mine. These detailed the depth of the scour pit, as well as the area of the pit flush with a level plane at multiple depths and the total volume scoured. The height of the mine exposed above the ambient seafloor was also measured.

These measurements detailed the progression of the scour pit during deployment of the mine. The conclusions obtained from these results reveal the mechanism detailing how the scour pit forms and the mine is subsequently buried. Orbital wave velocities associated with large storm events where significant wave heights are greater than 2 m create turbulent flow locally close to the mine. The turbulent boundary layer related to this turbulent flow entrains and suspends sediment out of the scour pit and into the water column, which is then transported out of the scour pit by weak preexisting currents. This develops the scour pit around the mine, expanding it in size and depth, while the mine remains sitting on a small pedestal of sand, elevated slightly above the deepest depths of the scour pit. After the storm has passed, the mine is then forced to roll off its pedestal, causing the mine to sink deeper below the far field seabed. Tidal and current flow dominants over orbital wave velocities during the calm period after a

storm. This drives sediment into the scour pit, decreasing its depth and size, and at the same time buries the mine. This process is repeated for each succeeding storm, sinking and burying the mine further below the ambient seafloor.

Mine percent burial by mine height exposure above the ambient seafloor was calculated as a characteristic value to describe the extent of the scour pit for operational mine hunting uses. The method is advantageous over other percent burial calculations using actual scour pit depths due to the tendency for scour to occur around the mine, but not immediately beneath it, leaving the mine slightly elevated on a small pedestal of sand. Percent burial by mine height translates much better to typical mine hunting methods, often with sidescan sonars.

The actual numerical values found in this analysis of scour-induced mine burial can be compared with the Office of Naval Research's Mine Burial Prediction model, as has already been done in coarse sand. When placed on a coarse sand bottom, mines have been seen to only partially bury, dropping below the ambient seafloor until the present approximately the same roughness as local bedforms nearby. This characteristic in coarse sand was able to be "tuned" into ONR's model, so that it could reflect this feature (Trembanis, et al. 2006; Traykovski et al. 2006). Similar model results to those presented here for mine deployments in fine sand will verify the model's accuracy, and speed its deployment and use in the mine hunting fleet. If the experimental and theoretical results do not match, then actual data can be used to fine-tune the model and allow for a more accurate theoretical model to be developed.

BIBLIOGRAPHY

- Austin, T. C., J. B. Edson, W. R. McGillis, M. Purcell, R. A. Petitt, M. K. McElroy, C. W. Grant, J. Ware, S. K. Hurst, 2002. A Network-Based Telemetry Architecture Developed for the Martha's Vineyard Coastal Observatory. *IEEE Journal of Oceanic Engineering* 27(2): 228-234.
- Goff, J. A., L. A. Mayer, P. A. Traykovski, I. Buynevich, R. H. Wilkens, R. Raymond, G. Glang, R. L. Evans, H. Olson, and C. Jenkins, 2005. Detailed investigation of sorted bedforms, or "rippled scour depressions," within the Martha's Vineyard Coastal Observatory, Massachusetts. *Continental Shelf Research* 25: 461-484.
- Gordon, M. R. and B. E. Trainor, 1995. *The General's War: The Inside Story of the Conflict in the Gulf*. New York, Little, Brown, and Company.
- Grant, W. D. and O. S. Madsen, 1979. Combined Wave and Current Interaction with a Rough Bottom. *Journal of Geophysical Research* 84: 1797-1808.
- Griffin, S., J. Bradley, M. Thiele, C. Tran, and F. Grosz, 2003. An Improved Subsequent Burial Instrumented Mine. *Sea Technology* 44(11): 40-44.
- Haas, K. A. and D. M. Hanes, 2004. Process Based Modeling of Total Longshore Sediment Transport. *Journal of Coastal Research* 20(3): 853-861.
- Highlights of the 6th International Symposium on Technology and the Mine Problem, 2004. MINWARA News.
- Inman, D. L., and S. A. Jenkins, 2002. *Scour and Burial of Bottom Mines: A Primer for Fleet Use*. Scripps Institution of Oceanography, SIO Reference Series No. 02-8.
- Mulhearn, P. J., 1996. A Mathematical Model for Mine Burial by Underwater Sand Dunes. Naval Postgraduate School, NPS Report No. DSTO-TR-0290, NPS Accession No. AD-A307-307.

- Richardson, M. D., G. R. Bower, K. B. Briggs, P. A. Elmore, C. S. Kennedy, P. J. Valent, D. F. Naar, S. D. Locker, P. Howd, A. C. Hine, B. T. Donahue, J. Brodersen, T. F. Wever, R. Luehder, C. T. Friedrichs, A. C. Trembanis, S. Griffin, J. Bradley, and R. H. Wilkens, 2004. Mine Burial by Scour: Preliminary Results from the Gulf of Mexico. *Proceedings of the Oceans 2003 Marine Technology and Ocean Science Conference*. San Diego, California, 22-26 September, 2003.
- Richardson, M. D., and P. A. Traykovski, 2002. Real-Time Observations of Mine Burial at the Martha's Vineyard Coastal Observatory. *Proceedings of the Fifth International Symposium on Technology and the Mine Problem*. Naval Postgraduate School, Monterey, California, 22-25 May 2002.
- Richardson, M. D., P. J. Valent, K. B. Briggs, J. Bradley, and S. Griffin, 2001. NRL Mine Burial Experiments. *Proceedings of the Second Australian-American Joint Conference on Technologies of Mine Countermeasures*. Defense Science and Technology Organization, Sydney, Australia, 27-29 March 2001.
- Sorensen, R. M., 1978. Basic Coastal Engineering. New York, John Wiley and Sons.
- Traykovski, P.A., M. D. Richardson, J. A. Goff, L. A. Mayer, R. H. Wilkens, and B. R. Gotowka, 2004. Mine burial experiments at the Martha's Vineyard Coastal Observatory. *Proceedings of the Sixth International Symposium on Technology and the Mine Problem*. Naval Postgraduate School, Monterey, California, 9-13 May 2004.
- Traykovski, P. A., M. D. Richardson, L. A. Mayer, and J. D. Irish, 2006. Mine burial experiments at the Martha's Vineyard Coastal Observatory. *IEEE Journal of Oceanic Engineering* **in publication**.
- Trembanis, A. C., C. T. Friedrichs, M. D. Richardson, P. A. Traykovski, P. A. Howd, P. A. Elmore, and T. F. Waver, 2006. Predicting Seabed Burial of Cylinders by Wave-Induced Scour: Application to the Sandy Inner Shelf off Florida and Massachusetts. *IEEE Journal of Oceanic Engineering* **in publication**.
- Voropayev, S. I., F. Y. Testik, H. J. S. Fernando, and D. L. Boyer, 2003. Burial and scour around short cylinder under progressive shoaling waves. *Ocean Engineering* 30: 1647-1667.

Zhao, Q and J. T. Kirby, 2005. Bagnold Formula Revisited: Incorporating Pressure Gradient Into Energetics Models. *The Fifth International Symposium on Ocean Wave Measurements and Analysis*. Madrid, Spain, 3-7 July 2005 **in publication**.